

Unveiling large-scale rotational motions in the intragroup medium at $z \sim 1$ through gravitational-arc tomography[★]

Cédric Ledoux^{1,★★}, Fernanda Muñoz-Olivares^{1,2}, L. Felipe Barrientos², Nicolas Tejos³, Trystyn Berg⁴, Felipe Corro-Guerra⁵, Evelyn Johnston⁶, Guillaume Mahler⁷, Jorge González-López², Joaquín Hernández-Guajardo², and Pasquier Noterdaeme^{8,9}

¹ European Southern Observatory, Alonso de Córdova 3107, Vitacura, Casilla 19001, Santiago, Chile

² Instituto de Astrofísica, Pontificia Universidad Católica de Chile, Casilla 306, Santiago, Chile

³ Instituto de Física, Pontificia Universidad Católica de Valparaíso, Casilla 4059, Valparaíso, Chile

⁴ Department of Physics and Astronomy, Camosun College, 3100 Foul Bay Road, Victoria, BC, Canada V8P 5J2

⁵ Centre de Recherche Astrophysique de Lyon, UMR5574, 9 avenue Charles André, 69230 Saint-Genis-Laval, France

⁶ Instituto de Estudios Astrofísicos, Universidad Diego Portales, Av. Ejército Libertador 441, Santiago, Chile

⁷ STAR Institute, Quartier Agora, Allée du Six Août, 19c B-4000 Liège, Belgium

⁸ Institut d'Astrophysique de Paris, UMR7095, 98bis boulevard Arago, 75014 Paris, France

⁹ French-Chilean Laboratory for Astronomy, IRL3386, CNRS and U. de Chile, Casilla 36-D, Santiago, Chile

Received 27 February 2026 / Accepted 12 March 2026

ABSTRACT

Context. The circumgalactic medium (CGM) is a crucial interface between galaxies and their large-scale environment, regulating gas accretion and feedback processes. Yet, its physical and kinematic properties within galaxy groups, where most galaxies reside, remain poorly constrained.

Aims. We present the first spatially resolved characterisation of the cool intragroup medium (IGrM) in a spectroscopically confirmed galaxy group at $z \approx 1.167$, using absorption-line spectroscopy along multiple sightlines.

Methods. Using 30 independent sightlines towards the gravitationally lensed galaxy SGAS J003341.5+024217, we combine background light from an extended gravitational arc and various sources in the field to map the distribution and kinematics of diffuse, metal-enriched gas pertaining to this group.

Results. We detect prominent Mg II, Fe II, Ca II, and Mg I absorption extending up to a projected distance of 62 kpc from a massive ($\log M_{\star} = 11.0 \pm 0.1 M_{\odot}$) star-forming spiral and its interacting companion. Together with four other members, these form a compact group with a virial radius of 313 kpc. Down-the-barrel, blueshifted absorption indicates outflows. The distribution and two-dimensional kinematics of this gas suggest the influence of both tidal stripping and star formation-driven winds. Intervening absorption across the field partly traces internal galaxy motions. A simple superposition of individual discs cannot reproduce the velocity field at large impact parameters or in counter-rotating regions, while a global IGrM halo with a rotational velocity of $\approx 130 \text{ km s}^{-1}$ provides a good match. Beyond individual galaxy envelopes, the data are found to be consistent with a group-scale structure that co-rotates in concert with the galaxies. Assuming dynamical equilibrium, we estimate a total (cool+warm+hot) gas mass of $1.3 - 2.5 \times 10^{11} M_{\odot}$, with large systematic uncertainties, corresponding to roughly 50% of all baryons, within one-quarter of the group's virial radius.

Conclusions. These results point to a multiphase IGrM in which cool ($\sim 10^4 \text{ K}$) clouds are embedded within a dynamically coherent, group-wide halo. The gas appears gravitationally bound to the group rather than reaccreting onto individual galaxies. High-redshift strong Mg II absorbers may thus trace shared, metal-enriched halos shaped by galaxy interactions and feedback, with stripped and outflowing gas accumulating in the IGrM over time.

Key words. quasars: absorption lines – galaxies: halos – galaxies: interactions – galaxies: clusters: individual (SGAS J003341.5+024217)

1. Introduction

The diffuse gas component of the Universe plays a central role in the formation of galaxies and drives their evolution across cosmic time. In this context, the circumgalactic medium (CGM) serves as a transition region between the pervasive cosmic web on megaparsec scales and the in-

ner star-forming regions of galaxies (Tumlinson et al. 2017; Péroux & Howk 2020). Numerical simulations predict that cool gas streams from the large-scale structures become collimated and contribute to generating angular momentum within the CGM, a phenomenon still poorly constrained observationally (e.g., DeFelippis et al. 2020, 2021). In addition, metal-enriched gas and dust produced by star formation can be expelled from galaxies to the CGM through powerful stellar winds and active galactic nuclei (AGN), as well as processes such as tidal and ram-pressure stripping.

[★] Based on observations carried out in service mode at the European Southern Observatory (ESO) under programme ID 098.A-0459(A).

^{★★} Corresponding author: cledoux@eso.org

This leads to a complex interplay between various gaseous phases (see [Faucher-Giguère & Oh 2023](#)).

Diffuse gas can be studied through absorption lines detected against background sources such as quasars and γ -ray burst afterglows. Modern spectroscopic quasar surveys routinely identify systems with large neutral-hydrogen column densities at intermediate and high redshifts, known as damped Lyman- α absorbers (DLAs), as well as strong Mg II systems (e.g., [Noterdaeme et al. 2009](#); [Chabanier et al. 2022](#)). These absorbers are believed to originate from gas associated with galaxies, as indicated by their significant metal content. DLAs usually consist of a mixture of warm and cool ($\sim 10^4$ K) gas with low average molecular fractions ([Ledoux et al. 2003](#); [Noterdaeme et al. 2008](#)). Due to these characteristics and the preferential selection of absorbers at large galactocentric distances, the bulk of the gas traced by metal-rich quasar absorbers is more likely located in the outskirts of galaxies than in the most central regions of star formation (e.g., [Krogager et al. 2012](#); [Muzahid et al. 2015](#); [Neeleman et al. 2025](#)).

To date, cool gas in the CGM at $z \sim 1$ has predominantly been studied using Mg II absorption by leveraging the statistical power of numerous, randomly distributed quasar sightlines. For example, [Huang et al. \(2021\)](#) showed that the rest-frame equivalent width of the Mg II $\lambda 2796$ line depends, on average, on the halo radius, B-band luminosity, and stellar mass of the galaxies associated with the absorption. The covering fraction of Mg II-bearing gas is typically high, exceeding 60% within 40 kpc of isolated galaxies, and it declines rapidly, vanishing beyond projected distances of $\gtrsim 100$ kpc. However, while quasar sightlines provide valuable insights, they remain sparse and usually offer a single pencil beam per field (e.g., [Weng et al. 2023](#)). As such, complementary constraints from individual halos are needed to fully understand the properties of the CGM.

To investigate the CGM of individual galaxies or galaxies in groups, [Lopez et al. \(2018\)](#) pioneered a technique known as gravitational-arc tomography (hereafter referred to as ARCTOMO). This approach utilises integral-field spectroscopic observations of the brightest known extended gravitational arcs in the sky, providing multiple, contiguous or closely spaced, sightlines within each field. This represents an advancement in CGM studies, as it enables detailed examinations of gas distributions around galaxies and spatially resolved measurements of velocity fields within individual halos ([Lopez et al. 2020](#); [Mortensen et al. 2021](#); [Fernandez-Figueroa et al. 2022](#); [Bordoloi et al. 2022](#)). To date, such studies have revealed a complex picture, in which metal-enriched gas exhibits clumpy distributions (e.g., [Afruni et al. 2023](#)) and/or co-rotates with stellar discs out to distances of tens of kiloparsecs ([Lopez et al. 2020](#); [Tejos et al. 2021](#)). Additionally, observations of outflows provide insights into metal recycling processes within the CGM (e.g., [Nielsen et al. 2020](#); [Tejos et al. 2021](#)).

In this paper, we use ARCTOMO to explore the kinematics of DLA-like gas in the vicinity of galaxies in groups, where dynamical effects are expected, extending our analysis of the CGM to the IGrM. We present Very Large Telescope (VLT) observations of the bright lensed galaxy SGAS J003341.5+024217 (hereafter SGAS J0033+02), integrating emission and absorption line data to constrain both the distribution and kinematics of diffuse, metal-enriched gas traced by Mg II absorption, within a galaxy group at $z \approx 1.17$. Throughout this work, we adopt a

spatially flat Λ CDM cosmology with $\Omega_m = 0.3$ and $H_0 = 70$ km s $^{-1}$ Mpc $^{-1}$.

2. Observations

2.1. Target selection and HST/WFC3 imaging

The bright lensed galaxy SGAS J0033+02 at $z \approx 2.39$ was discovered during a survey aimed at identifying giant, bright gravitational arcs, which contributed to creating the Magellan Evolution of Galaxies Spectroscopic and Ultraviolet Reference Atlas, known as MEGaSAURA ([Rigby et al. 2018](#)). In the spectrum of this source, strong Mg II absorption lines were detected at $z \approx 1.17$ within the arc continuum emission, leading us to identify this field as a target for gravitational-arc tomography.

The field of SGAS J0033+02 was previously observed with the Wide Field Camera 3 onboard *HST* during two visits on October 30 and November 8, 2016 (proposal ID 14170; PI: Wuyts). In the IR channel, images were captured using the F105W and F140W filters, while in the UVIS channel, exposures were taken with the F410M, F555W, and F814W filters. The observations and data reduction procedures are described in [Fischer et al. \(2019\)](#).

[Fig. 1](#) shows a multi-colour *HST* composite image of the field, spanning the optical to near-infrared range. The lensing model presented in [Fischer et al. \(2019\)](#) revealed a system comprising one main gravitational arc and two counter-images of the lensed galaxy. The foreground lensing, massive galaxy cluster is located at $z = 0.4716$. Additionally, ALMA 870 μ m observations by [Solimano et al. \(2021\)](#) detected dust-continuum emission from a prominent galaxy in the field, which we will refer to as ‘‘G1’’.

2.2. VLT/MUSE integral-field spectroscopy

Follow-up observations of SGAS J0033+02 were conducted at the VLT as part of ESO programme ID 098.A-0459(A) (PI: Lopez) using the Multi-Unit Spectroscopic Explorer (MUSE; [Bacon et al. 2010](#)). MUSE is an optical integral-field spectrograph with a $1' \times 1'$ field of view in its Wide-Field mode and a native spatial (spaxel) scale of $0''.2$. The instrument yields a resolving power of $R \sim 1770$ at 480 nm and $R \sim 3590$ at 930 nm.

The data were acquired in natural-seeing mode during dark time on the nights of September 19 and 20, 2017. Throughout the observations, the seeing conditions at the zenith remained stable at $0''.6$ FWHM, as measured by the Differential Image Motion Monitor (DIMM) in V-band. The sky transparency conditions were photometric, and the target airmass ranged from 1.15 to 1.5 during the observations. A total of eleven exposures were obtained, each with an integration time of 701 s, distributed across three observing blocks. To minimise flux variations among the different slicers and channels of the instrument in the combined datacube, the telescope pointing was slightly offset, and the instrument’s position angle on the sky was rotated by 90° between each exposure. During each night, a spectrum of the standard star HD 49798 was recorded, also under photometric conditions.

The data reduction was performed using the MUSE pipeline v2.2 ([Weilbacher et al. 2020](#)) within the ESO Recipe EXecution tool (EsoRex) environment ([ESO CPL Development Team 2015](#)). Wavelengths in the

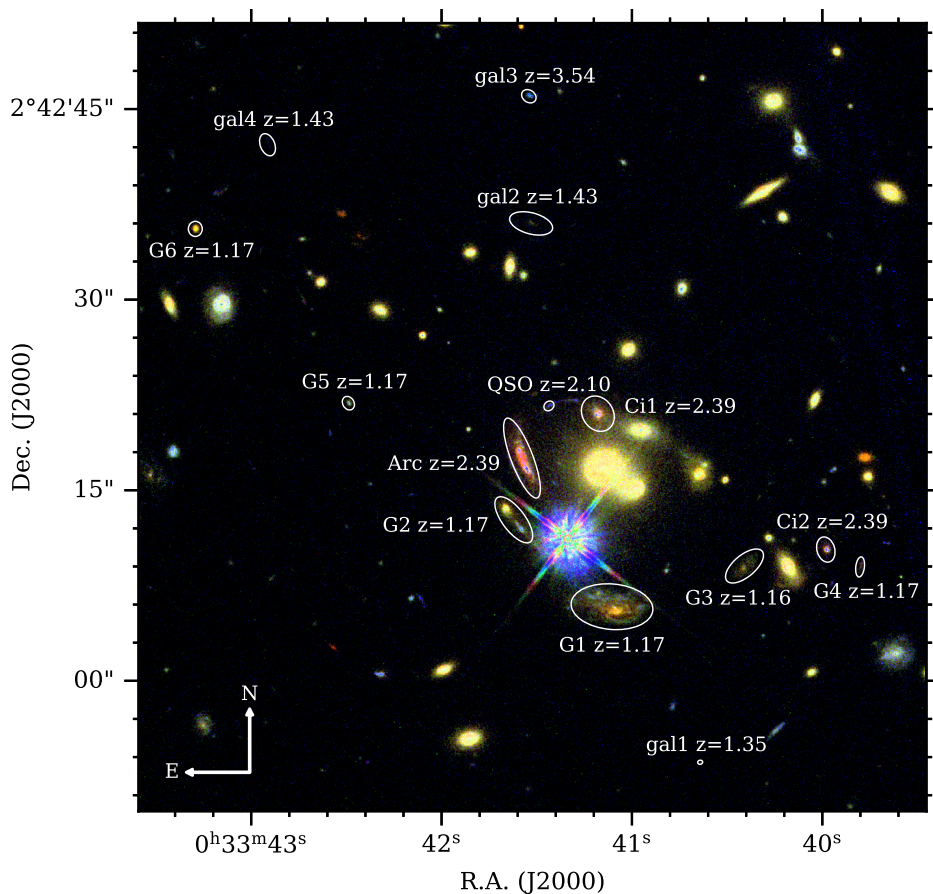


Fig. 1. Field of SGAS J0033+02 observed with *HST* in the optical (F814W) and near-infrared (F105W and F140W) bands. The gravitational arc formed by the lensed galaxy at $z \approx 2.39$ (called the 'Arc') and its counter-images ('Ci1' and 'Ci2') are indicated. The bluish object located $7''.3$ southwest of the arc is a Galactic star. The main absorbing galaxy at $z \approx 1.17$, labelled 'G1', is shown along with its closest two companions at the same redshift: 'G2' to the northeast, and 'G3' to the west. Redshifts for these and additional sources at $z > 1.16$ are indicated next to each label.

observer's frame were converted to vacuum and corrected to the solar-system barycentre. The standard-star frames were processed to derive flux calibration solutions, and the sky background was measured in each science exposure using regions of the field of view free of light contamination. Flux calibration and sky subtraction were applied to the science frames during post-processing, and the reduced pixel tables from each exposure were combined to produce a stacked datacube. The absolute spectro-photometric accuracy is approximately 0.05 mag.

Finally, the residuals from sky emission lines were removed using the Zurich Atmosphere Purge (ZAP) algorithm (Soto et al. 2016), and the MUSE data product was aligned to match the astrometry of the *HST* images. The astrometric registration was performed by identifying compact sources common to both the MUSE white-light image and the *HST* F814W image. A small rigid 2D shift ($\leq 0''.2$) was applied to the MUSE datacube World Coordinate System, yielding a relative astrometric accuracy between MUSE and *HST* of better than $0''.1$.

3. Image plane and lensing model

3.1. Galaxy census

We conducted a blind survey for galaxies within the MUSE field of view. Preliminary source identifications were performed on the deep $1.4\text{-}\mu\text{m}$ (F140W) *HST* image using the Source Extractor and Photometry software (Bertin & Arnouts 1996; Barbary 2018). We extracted 1D spectra from the MUSE datacube for each identified source using PyMUSE (Pessa et al. 2020). Due to field crowding,

particularly the presence of a foreground cluster cD elliptical and a Galactic star to the southeast of it, we estimated the diffuse background light, using concentric elliptical apertures around each source. The light was interpolated to the object inner region and subtracted from the flux in each object spaxel before extracting their spectra. To produce a combined 1D spectrum, we weighted each spaxel by their total integrated flux over the full MUSE wavelength range, using the white-weighted mean option of PyMUSE.

We also searched for $[\text{O II}]\lambda\lambda 3727, 3729$ emission lines across the field at approximately the redshift of the Mg II absorption lines detected in the MEGA SaURA spectrum. This was done by constructing a MUSE narrow-band image (70 \AA wide, corresponding to $\approx 2600\text{ km s}^{-1}$ at $z = 1.17$) centred on the redshifted $[\text{O II}]$ doublet. We detected six $[\text{O II}]$ -emitting galaxies at $z \approx 1.17$, two of which show weak or no continuum emission. All of these galaxies have counterparts in the *HST* optical images, indicating that none were missed in the earlier source identification. We label them G1, G2, G3, G4, G5, and G6, in order of increasing projected distance from G1. As shown in Fig. 1, these galaxies are roughly aligned on the sky, suggesting the presence of a large-scale filamentary structure. G1, the largest and most massive galaxy in the group (see Sect. 4.1), lies near the centre of the field. Its closest companion, G2, is located approximately $10''$ to the northeast of G1. The remaining four galaxies are distributed on either side of the G1-G2 pair.

All sources identified at $z \geq 1.17$, relevant to the analysis of gaseous absorption at $z \approx 1.17$, are listed in Table 1. Object classifications and, where available, redshifts

Table 1: Census of extragalactic sources at $z > 1.16$.

Object	MARZ classification	z^a	Lines used	R.A. ^b (J2000)	Dec. ^b (J2000)	$\theta^{b,c}$ [$''$]	Mg II at $z_{\text{abs}} \approx 1.17?$
Group galaxies at $z \approx 1.17$:							
G1	Late type emission galaxy	1.1672(3)	[O II]	0 ^h 33 ^m 41 ^s :10	+2° 42' 5''6	0.0	Yes ^d
G2	Star-forming galaxy	1.1674(0)	[O II]	0 ^h 33 ^m 41 ^s :61	+2° 42' 12''7	10.43	Yes ^d
G3	Late type emission galaxy	1.1649(9)	[O II]	0 ^h 33 ^m 40 ^s :40	+2° 42' 9''1	11.06	Yes ^d
G4	Star-forming galaxy	1.1667(6)	[O II]	0 ^h 33 ^m 39 ^s :79	+2° 42' 9''1	19.94	... ^e
G5	Late type emission galaxy	1.1674(5)	[O II]	0 ^h 33 ^m 42 ^s :48	+2° 42' 22''0	26.39	No
G6	Transitional galaxy	1.1673(8)	[O II]	0 ^h 33 ^m 43 ^s :28	+2° 42' 35''7	44.42	... ^e
Lensed galaxy SGAS J0033+02:							
Arc	High- z star-forming galaxy	2.3874	C III]	0 ^h 33 ^m 41 ^s :57	+2° 42' 17''6	13.91	Yes
Ci1	High- z star-forming galaxy	2.3874	C III]	0 ^h 33 ^m 41 ^s :17	+2° 42' 21''1	15.54	Yes
Ci2	High- z star-forming galaxy	2.3874	C III]	0 ^h 33 ^m 39 ^s :97	+2° 42' 10''5	17.63	Yes
Additional sources:							
gal1	Transitional galaxy	1.3510(7)	[O II]	0 ^h 33 ^m 40 ^s :63	+2° 41' 53''7	13.83	... ^e
QSO	Quasar	2.0966	C III]	0 ^h 33 ^m 41 ^s :43	+2° 42' 21''7	16.84	Yes
gal2	Transitional galaxy	1.4300(3)	[O II]	0 ^h 33 ^m 41 ^s :52	+2° 42' 36''1	31.14	No
gal3	High-redshift galaxy	3.5421:	H I, C IV ^f	0 ^h 33 ^m 41 ^s :53	+2° 42' 46''1	41.01	No
gal4	Transitional galaxy	1.4308(3)	[O II]	0 ^h 33 ^m 42 ^s :90	+2° 42' 42''3	45.54	... ^e
gal5	Star-forming galaxy	1.4312(8)	[O II]	0 ^h 33 ^m 43 ^s :66	+2° 42' 52''4	60.51	... ^e

Notes. (a) Redshift derived from integrated spectra; (b) Image plane; (c) Angular distance from G1; (d) Down-the-barrel absorption; (e) Faint continuum; (f) Absorption lines.

were determined using the template-matching algorithm MARZ (Hinton et al. 2016). In addition to the gravitational arc (hereafter referred to as “the Arc”) and the two counter-images (Ci1 and Ci2) of the $z \approx 2.39$ lensed galaxy SGAS J0033+02, the field contains a quasar at $z = 2.0966$, located approximately $5''$ north of the Arc, and five additional galaxies (labelled with the prefix ‘gal’), primarily at $z \approx 1.43$.

3.2. Lensing model and connection between G1 and G2

G1 is a spiral galaxy, whose image is distorted by gravitational lensing. This effect, caused by the massive foreground galaxy cluster, stretches the images and amplifies their luminosities. To recover an accurate representation of G1 and other sources at the absorber’s redshift, we developed a lens model for SGAS J0033+02 using the `Lenstool` software (Jullo et al. 2007), constrained by the *HST* imaging. The model, described in Fischer et al. (2019) and available upon request, allows us to reconstruct the true positions of the sources in the absorber plane by ray tracing through the lens equation. The relative accuracy of the reconstructed positions varies across the field due to the gradient in magnification, resulting in an uncertainty of 10% in the calculated impact parameters. This level of uncertainty is typical of ARCTOMO studies (e.g., Tejos et al. 2021). The magnification map at the absorber redshift of $z = 1.17$ is shown in Fig. B.1.

Applying the deflection matrices to the *HST* F140W image recovers the absorber-plane geometry shown in Fig. 2. This reveals that G1 and G2 are closely aligned in projection, with a separation of less than 15 kpc, and appear less elongated than in the image plane. The high-resolution *HST* image shows a double-peaked light profile in G2, which is more compact than the extended, diffuse emission from G1. Due to the dazzling glare of the Galactic star partially ob-

scuring this region, the presence of a bridge of matter connecting the two galaxies is not immediately apparent (see Sect. D). Nevertheless, G2 is likely an interacting companion of G1. The approximate alignment of their delensed images, along with the presence of a bar in G1’s core, strongly supports this interpretation (see Fig. 2).

4. Emission properties of group galaxies

To characterise the group at $z \approx 1.17$, we first combined the *HST* and MUSE datasets to constrain the stellar masses, star formation rates, and disc properties of the individual galaxies.

4.1. Stellar masses

We determined the stellar mass of each galaxy from the combination of *HST* photometry and MUSE continuum spectra. For this, we employed the Bayesian Analysis of Galaxies for Physical Inference and Parameter ESTimation software, `Bagpipes` (Carnall et al. 2018, 2019). *HST* magnitudes were measured in the image plane and corrected for Galactic extinction (Schlafly & Finkbeiner 2011). The stellar population models used in `Bagpipes` were the 2016 versions of the Bruzual & Charlot (2003) models, incorporating the stellar initial mass function (IMF) of Kroupa (2001). Star-formation histories were modelled as double-power-laws following Behroozi et al. (2013). After correcting for a median magnification factor of $\mu = 5.6$ (see Table 2),¹ we inferred a stellar mass of $\log(M_{\star}/M_{\odot}) =$

¹ Since our SED fitting uses integrated photometry and spectra, the derived quantities represent magnification-weighted averages. Differential lensing could introduce systematic uncertainties in stellar mass and SFR estimates when the magnification varies across a galaxy’s image (see Fig. B.1). For G1, the gradi-

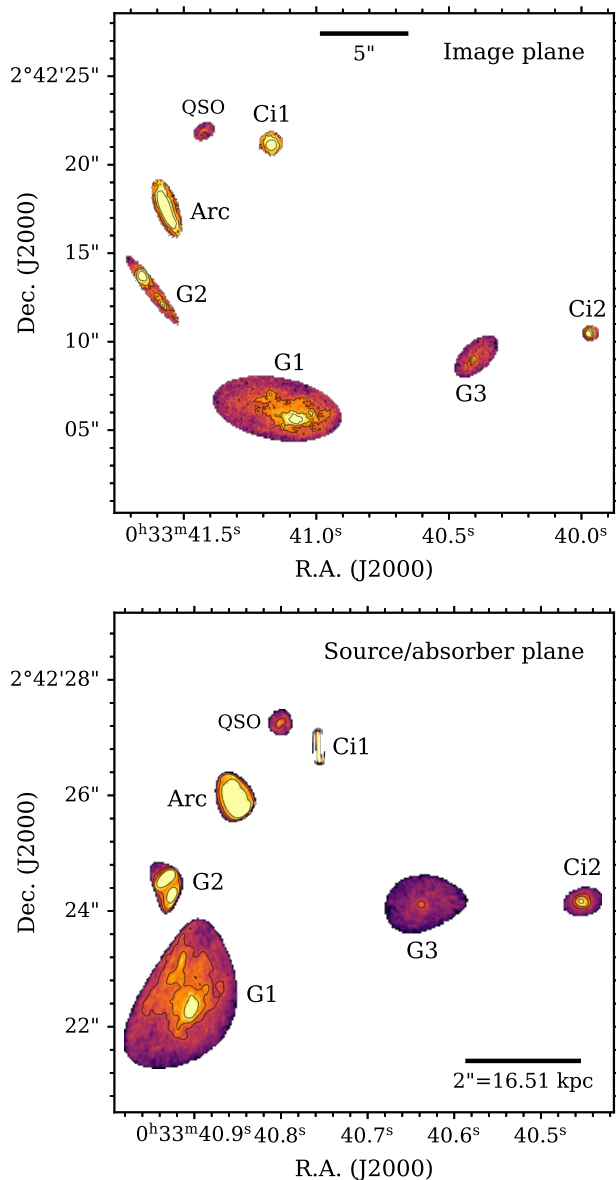


Fig. 2: Brightest sources at $z > 1.16$ near the centre of the foreground galaxy cluster observed in *HST* F140W imaging. Black contours trace the flux distribution in the image. The *upper panel* shows the image plane, while the *lower panel* displays the delensed absorber plane at $z = 1.17$. The elliptical aperture around G1 includes its eastern region, which is stretched by gravitational lensing.

11.01 ± 0.08 for G1. Based on the stellar-to-halo mass relation of [Moster et al. \(2010\)](#), this corresponds to a virial radius of $R_{200} = 271 \pm 33$ kpc. We applied the same methodology to the other identified group members. Our results are summarised in [Table 2](#).

From this, we conclude that G1 and G3 are the most massive galaxies in the group and that the virial radii of

ents are typically of order 20-30% across its extent. We estimate this introduces a small systematic uncertainty of ~ 0.1 dex in stellar mass, which is comparable to the statistical uncertainties reported in [Table 2](#). The impact on G1's SFR estimate is similar, as both stellar mass and [O II]-based SFRs are corrected using the same median magnification factor. Such systematic effects are much smaller for the less extended G2 to G6 galaxies.

all galaxies, except G6, overlap, indicating a bound structure. It remains to be assessed whether each galaxy in this structure maintains its own CGM or shares a common halo.

4.2. Star-formation rates

To derive star-formation rates (SFRs), we used the Python Spectroscopic Analysis and Plotting package, *PySpecKit* ([Ginsburg et al. 2022](#)). We fitted the [O II] $\lambda\lambda 3727, 3729$ emission line doublet in the previously extracted MUSE spectra of G1 to G6 using double Gaussian profiles on top of normalised continua (see [Fig. C.1](#)). The measured fluxes were corrected for gravitational magnification, Galactic extinction at the observed wavelengths (using the reddening maps from [Schlafly & Finkbeiner 2011](#)), and internal galaxy extinction at rest-frame wavelengths assuming the [Calzetti et al. \(2000\)](#) extinction law for starbursts and the internal extinction in *V* band, A_V , derived from *Bagpipes* (see [Sect. 4.1](#)). The total [O II] luminosities were converted to SFRs following [Davies et al. \(2016\)](#), but assuming the IMF of [Kroupa \(2001\)](#), using the following relation:

$$\text{SFR}_{[\text{OII}]} (M_{\odot} \text{ yr}^{-1}) = 1.1 \times 10^{-41} L_{[\text{OII}]} (\text{erg s}^{-1}). \quad (1)$$

When converting the observed luminosities to intrinsic values, we applied an offset of 0.1 dex towards lower metallicities at $z \approx 1$ relative to the local mass-metallicity relation (e.g., [Lara-López et al. 2013](#); [Sanders et al. 2021](#)). Our results are summarised in [Table 2](#). For G1, we derived an unobscured SFR of $70.0 \pm 1.6 M_{\odot} \text{ yr}^{-1}$. For comparison, G1's integrated SFR based on SED fitting (see [Sect. 4.1](#)) is $63.7 \pm 0.1 M_{\odot} \text{ yr}^{-1}$. These differences are expected, as instantaneous SFR traces recent star formation over ~ 10 Myr, while SED fitting averages over longer timescales (≥ 100 Myr; e.g., [Kennicutt & Evans 2012](#)). For the other five galaxies, the two methods yield results differing by up to 30%, typically indicating enhanced recent star formation activity.

Most galaxies in the group follow the main sequence of star formation, which links the star-formation rate to the stellar mass, at intermediate redshifts (e.g., [Bauer et al. 2005](#)). However, G1 is positioned at the high end of the SFR distribution for its relatively large stellar mass. Its specific SFR is 0.69 Gyr^{-1} – a factor of 20 higher than the galaxy main sequence at $z = 1.2$ ([Bauer et al. 2005](#)) and three times higher than the average starburst galaxy at that redshift ([Atek et al. 2014](#); [Pearson et al. 2018](#)). Given G1's unique configuration within the group, it appears to be experiencing a starburst phase driven by a small number of massive star-forming regions. These clumps are likely the result of violent disc instabilities triggered by interactions (e.g., [Elmegreen et al. 2009](#); [Puschnig et al. 2023](#)).

4.3. Morpho-kinematics of [O II] emission

The ubiquity of [O II] emission among the galaxies in this group provides a valuable opportunity to study the kinematics of ionised gas directly associated with star formation. Unlike the other group members, G1, G2, and G3 are spatially resolved and extended enough to allow for the extraction of meaningful kinematic data. To model their dynamics, we employed the Galaxy Parameters and Kinematics from 3-Dimensional data software, *GalPak*^{3D} ([Bouché et al. 2015](#)), fitting the MUSE data using single rotating disc models characterised by an exponential

Table 2: Galaxy masses and star-formation rates.

	$\log(M_{\star}/M_{\odot})^a$	$\log(M_{\text{h}}/M_{\odot})$	R_{vir} [kpc]	SFR_{SED}^a [$M_{\odot} \text{ yr}^{-1}$]	$A_{\text{V}}^{a,b}$ (mag)	μ^c	$f_{[\text{O II}]}^{d,e}$	$SFR_{[\text{O II}]}^f$ [$M_{\odot} \text{ yr}^{-1}$]
G1	11.01 ± 0.08	12.93 ± 0.16	271 ± 33	63.7 ± 0.1	1.13	5.6	842 ± 19	70.0 ± 1.6
G2	10.14 ± 0.06	11.96 ± 0.03	129 ± 3	4.9 ± 0.1	0.38	10.5	66.9 ± 0.6	4.7 ± 0.1
G3	10.56 ± 0.12	12.26 ± 0.12	162 ± 14	13.4 ± 0.1	1.42	3.7	216 ± 8	17.4 ± 0.7
G4	9.56 ± 0.18	11.69 ± 0.08	105 ± 6	1.4 ± 0.6	0.68	2.1	32.4 ± 2.1	1.8 ± 0.2
G5	9.44 ± 0.16	11.64 ± 0.07	101 ± 5	17.7 ± 0.2	1.71	2.1	386 ± 7	19.7 ± 0.4
G6	10.22 ± 0.22	12.00 ± 0.13	134 ± 13	1.3 ± 1.4	0.34	1.5	23.9 ± 1.3	1.7 ± 0.1

Notes. ^(a) Derived from SED fitting; ^(b) Internal extinction in V band; ^(c) Median magnification factor; ^(d) [O II] flux corrected for gravitational magnification, Galactic extinction, and internal extinction; ^(e) In units of $10^{-18} \text{ erg s}^{-1} \text{ cm}^{-2}$; ^(f) Star-formation rate based on [O II] emission.

Table 3: Morpho-kinematic analysis of [O II] emission.

	Coords. R.A. & Dec. ^a (J2000)	$\text{PA}_{\text{gas}}^{a,b}$ [$^{\circ}$]	i_{gas}^a [$^{\circ}$]	$r_{\frac{1}{2}}^{a,c}$ [kpc]	z_{sys}	$v_{\text{rot,gas}}^{a,d}$ [km s^{-1}]	$\sigma_{v,\text{gas}}^{a,d}$ [km s^{-1}]
G1	$0^{\text{h}}33^{\text{m}}40^{\text{s}}90 + 2^{\circ}42'22''2^e$	149.1 ± 0.5	49.5 ± 4.7	7.4 ± 0.01	1.16666	276.8 ± 2.1	26.2 ± 2.5
G2	$0^{\text{h}}33^{\text{m}}40^{\text{s}}92 + 2^{\circ}42'24''3^e$	43.8 ± 0.7	75.8 ± 0.6	1.6 ± 0.02	1.16745	142.2 ± 2.5	74.2 ± 1.0
G3	$0^{\text{h}}33^{\text{m}}40^{\text{s}}63 + 2^{\circ}42'24''1^e$	128.1 ± 2.7	42.0 ± 0.0^e	2.2 ± 0.09	1.16484	169.9 ± 5.1	$< 8.4^f$

Notes. ^(a) Delensed absorber plane; ^(b) Position angle of the approaching semi-major axis (east of north); ^(c) Half-light radius; ^(d) Assuming a rotation curve $v(r) = v_{\text{rot,gas}} \frac{2}{\pi} \arctan(r/r_i)$; ^(e) Fixed parameter; ^(f) Upper limit: the [O II] emission is unresolved at MUSE spectral resolution.

light profile, an arctangent rotation curve, and a Gaussian thickness profile. Following the methodology outlined in Tejos et al. (2021), we used the delensed [O II] emission-line MUSE datacube and an effective delensed PSF as input to GalPak^{3D}. The delensed cube was constructed at the absorber-plane redshift by applying the deflection matrices to the vertices of each spaxel, within a sub-cube of the original data, centred on each galaxy and with the spectral continuum subtracted. The spaxels in the delensed sub-cube were then resampled onto a regular $0.1 \times 0.1 \text{ arcsec}^2$ grid, consistent with the typical size of the delensed spaxels in the absorber plane. This regridding introduces correlations between adjacent spaxels in those regions or directions where delensing is negligible. This increases the noise correlation length but does not bias the derived kinematic parameters, as GalPak^{3D} samples the model at the native spaxel positions. The spaxel correlation therefore primarily affects the goodness-of-fit statistics rather than the best-fit parameters. Care was taken to define extraction regions around each galaxy, avoiding spaxels subject to strong tangential stretching, especially in the area between G1 and G2. The spatially variable PSF in the absorber plane was accounted for by providing GalPak^{3D} with the local effective PSF at each galaxy’s position. We verified that using a constant PSF changes the derived rotation velocities by less than 5 km s^{-1} , well within our reported uncertainties.

GalPak^{3D} was run to convergence for up to 10,000 iterations, yielding satisfactory kinematic solutions for all three galaxies. The modelling of G2, however, was subject to larger uncertainties owing to the limited number of available MUSE spaxels. To improve convergence, we fixed its central coordinates to the mid-point of the two brighter peaks in the delensed *HST* image. Note that, for illustrative purposes, the image of G2 in Fig. 2 is truncated; the galaxy extends slightly further to the south-west. For G1 and G3, we also fixed their central coordinates based on the delensed

HST image, while allowing all other parameters to vary, except the inclination of G3, which was determined from its major-to-minor axis ratio. However, these adjustments had only minor effects on the results. From these analyses, we derived the key disc parameters of each galaxy, including the systemic redshift (z_{sys}), maximum rotational velocity ($v_{\text{rot,gas}}$), and gas velocity dispersion ($\sigma_{v,\text{gas}}$), as summarised in Table 3. The systemic redshifts obtained with GalPak^{3D} are more accurate than those derived from simple Gaussian fits to the integrated [O II] emission lines (see Sect. 4.2) and are adopted hereafter. The inferred rotational velocities are consistent with expectations based on the galaxies’ masses. G1 and G3 exhibit well-ordered, star-forming discs, with large v_{rot}/σ_v ratios, whereas G2 shows signs of disturbed rotation, likely reflecting G1’s dynamical influence.

5. Absorption lines at $z \simeq 1.17$

With all relevant galaxy parameters established, we now turn to the central aim of this study: investigating the properties of cool-gas absorption within the group.

5.1. Down-the-barrel absorption

We find that half of the galaxies in the $z \simeq 1.17$ group display down-the-barrel (DtB) absorption, meaning that absorption is detected at approximately the same redshift as the galaxies themselves, superimposed on their continuum emission spectra (see Table 1). This absorption is most clearly observed towards G1 and G2, but is also present towards G3. Such features probe the CGM and/or IGrM located in front of each galaxy, as well as their interstellar media (ISM).

The DtB Mg II absorption is blueshifted with respect to the galaxies’ systemic redshifts, with velocity shifts of

Table 4: Absorption lines at $z \simeq 1.17$: properties from MUSE integrated spectra.

Object	Beam type	d_{proj}^a	Δv^b	σ_v^c	W_r^{2796}	$\frac{W_r(\lambda 2803)}{W_r(\lambda 2796)}$	$\frac{W_r(\lambda 2600)}{W_r(\lambda 2796)}$	$\frac{W_r(\lambda 2852)}{W_r(\lambda 2796)}$
		[kpc]	[km s $^{-1}$]	[km s $^{-1}$]	[Å]			
G1	DtB/extended	15.1	-21 ± 10	151 ± 9	3.61 ± 0.32	1.11 ± 0.14	0.99 ± 0.16	0.28 ± 0.07
G2	DtB/extended	4.9	$+20 \pm 11$	156 ± 9	4.16 ± 0.40	1.02 ± 0.11	0.79 ± 0.15	0.63 ± 0.10
G3	DtB/extended	40.1	-30 ± 47	245 ± 36	4.63 ± 1.00	0.66 ± 0.23	0.70 ± 0.27	0.38 ± 0.16
G5	DtB/extended	64.6	$< 2.28^d$
Arc	extended	20.8	$+61 \pm 2$	150 ± 2	4.09 ± 0.05	0.99 ± 0.02	0.78 ± 0.02	0.35 ± 0.02
Ci1	extended	34.0	$+16 \pm 7$	134 ± 6	3.70 ± 0.15	0.98 ± 0.07	0.75 ± 0.09	0.36 ± 0.05
Ci2	extended	62.6	-33 ± 11	132 ± 11	3.54 ± 0.40	0.87 ± 0.14	0.46 ± 0.13	0.22 ± 0.08
QSO	point source	32.8	$+34 \pm 18$	71 ± 15	2.30 ± 0.39	1.00 ± 0.24	0.99 ± 0.47	0.55 ± 0.24
gal2	extended	95.2	$< 1.30^d$
gal3	~point source	163.5	$\leq 1.44^e$

Notes. ^(a) Projected distance from the group’s barycentre (absorber plane); ^(b) Relative to the mass-weighted mean redshift of the group ($z_{\text{sys}} = 1.16663$); ^(c) Deconvolved from the instrumental Line Spread Function ($\sigma_{\text{inst}} = 1.083 \text{ \AA}$ at $\lambda_{\text{obs}} = 6060 \text{ \AA}$); ^(d) 2σ upper limit; ^(e) Blend.

-40 ± 10 and $-94 \pm 11 \text{ km s}^{-1}$ for G1 and G2, respectively (see Table 4 and Fig. C.2). This indicates the presence of outflowing gas, possibly driven by star formation. However, the bulk of the absorption in front of G1, where the signal is better resolved than for G2, is not aligned with G1’s minor axis. Instead, it is predominantly oriented towards G2 (see Fig. D.2). This geometry suggests that gas is being stripped as a result of the interaction between the two galaxies, causing each to lose part of their gaseous reservoirs. Although the region between G1 and G2 is partly obscured by the glare of the Galactic star, there are also indications of a bridge of material traced by [O II] emission connecting the two galaxies (Figs. D.2). We interpret this as the region where material is transferred into their shared CGM. Shock-heated gas within tidal features is typically observed in interacting systems (e.g., Smith et al. 2010; Joshi et al. 2019). Therefore, while star-formation-driven winds (particularly from G1, given its elevated SFR) may contribute to the outflow, tidal stripping is likely to play a significant role in removing gas from these galaxies (see Sparre et al. 2022).

For G3, the DtB Mg II absorption exhibits a complex profile (see Fig. C.2), with an average velocity shift of $+208 \pm 47 \text{ km s}^{-1}$ relative to the galaxy’s systemic redshift. This positive offset cannot be attributed to outflowing gas. Instead, it shows that a significant fraction of the absorption originates at approximately the velocity of G1 ($+258 \text{ km s}^{-1}$ relative to G3), i.e., within the IGrM, as G3 moves towards the observer.

5.2. Intervening intragroup absorption

Intervening Mg II absorption towards sources at higher redshifts than the group itself pervades the field. Such absorption is detected towards all extragalactic background sources at $z > 1.17$, spanning projected distances from G1 of up to 70 kpc in the absorber plane (see Fig. C.2). Note that these sources preferentially probe regions along G1’s major axis.

Intervening Mg II absorption towards the Arc and its two counter-images, Ci1 and Ci2, are reminiscent of ultra-strong Mg II absorbers (e.g., Nestor et al. 2007, 2011; Rubin et al. 2010; Gauthier 2013; Nielsen et al. 2022;

Guha et al. 2024) observed towards quasars, with rest-frame equivalent widths of the Mg II $\lambda 2796$ line in excess of 3 \AA . This is surprising since a wide range of impact parameters from G1 are probed, i.e., between 30 and 60 kpc, in the delensed absorber plane. For sources farther than 70 kpc, only upper limits are derived. Line equivalent widths and ratios involving the Mg II $\lambda 2796$ line, derived from MUSE integrated spectra, are given in Table 4. The equivalent widths are subject to uncertainties related to the subtraction of diffuse background light around each source, which was performed during spectrum extraction (see Sect. 3.1). This introduces an additional uncertainty of up to 20% on the reported values.

In the spectrum of the Arc, we confirm the detection of Mg II $\lambda \lambda 2796, 2803$ and identified additional, prominent absorption lines at $z \simeq 1.1671$, i.e., Mg I $\lambda 2852$, Fe II $\lambda \lambda 2249, 2260, 2344, 2374, 2382, 2586, 2600$, and Ca II $\lambda \lambda 3934, 3969$. Neither Mn II $\lambda 2576$ nor Na I $\lambda 5891$ are detected. The strengths of the detected lines are reminiscent of what is observed in high-redshift quasar-DLAs. Berg et al. (2025) used Mg II metrics coupled with modelling to demonstrate that this system is indeed likely a DLA, with $\log N(\text{H I}) \simeq 20.6 \text{ cm}^{-2}$, and a covering fraction on top of the Arc of approximately 70%.

5.3. Spatially extended versus pencil-beam sightlines

Mg II absorption is detected at the 5σ confidence level in the spectrum of a quasar at $z \simeq 2.10$, located in projection near both the Arc and Ci1. The quasar sightline serves as a pencil beam probe, while the Arc and Ci1 correspond to spatially resolved, extended background sources. To our knowledge, this is the first time that both beam types can be compared at projected separations as small as 5–10 kpc, thereby probing the same physical environment.

The Mg II $\lambda \lambda 2796, 2803$ doublet in the quasar spectrum is saturated, as indicated by its equivalent-width ratio (see Table 4), consistent with what is observed in the spectra of the Arc and Ci1. After subtracting the diffuse background light around each source, the absorption troughs reach zero flux within the uncertainties of the subtraction process ($\sim 10\%$, or $\sim 20\%$ for the fainter quasar; see Fig. C.2). This

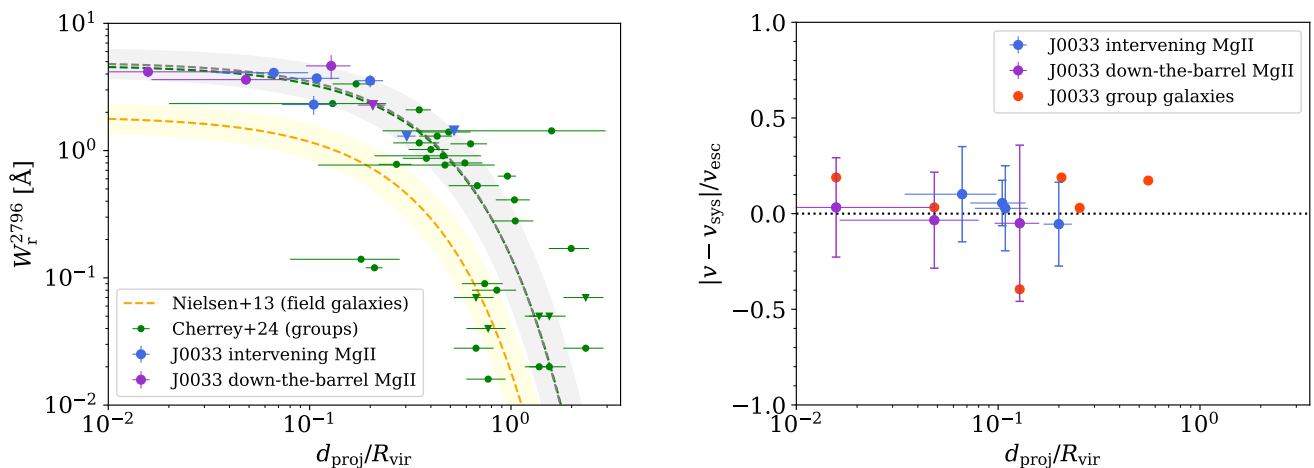


Fig. 3: *Left panel:* Rest-frame equivalent width of Mg II $\lambda 2796$ as a function of the projected distance from the group’s barycentre, normalised by the group’s virial radius. Our measurements are compared to the galaxy group sample from Cherrey et al. (2024). The overall best-fit relation for *intervening* Mg II absorption is displayed as a grey dashed line along with its 1σ confidence region. The original relation from Cherrey et al. (2024) is shown in green. *Right panel:* Velocity span of the Mg II profiles, $\Delta v \pm \sigma_v$, normalised by the group’s escape velocity, $v_{\text{esc}} = 601 \text{ km s}^{-1}$, as a function of the normalised projected distance from the group’s barycentre. The velocities of the individual galaxies are shown in red. The reference velocity, v_{sys} , is the mass-weighted mean redshift of the group ($z_{\text{sys}} = 1.16663$).

suggests no evidence for partial covering of the background sources by the Mg II-absorbing gas.

Both the equivalent widths and velocity widths of the Mg II lines are larger towards the extended sources (the Arc, Ci1, and Ci2) than along the quasar sightline. This comparison is based on a single quasar spectrum, whose limited S/N precludes a detailed analysis of line-profile shapes. Nevertheless, because ARCTOMO spectra are spatially averaged analogues of pencil-beam data, they are expected to provide a more global view of the intervening medium, with reduced sightline-to-sightline variations compared to quasars, particularly in the presence of clumpy gas distributions.

6. Results

6.1. Radial distribution of cool gas in groups

Cherrey et al. (2024) investigated intervening Mg II absorption along quasar sightlines in the vicinity of 26 galaxy groups, each containing more than five members, spanning redshifts $0.3 < z < 1.5$ and halo masses $10.7 < \log(M_{\text{h}}/M_{\odot}) < 13.7$. Out of 120 absorption systems, 21 were associated with such groups. They found that the typical impact parameter from the nearest galaxy, at which the Mg II covering fraction exceeds 50 per cent, is about three times larger than that for field galaxies. This indicates the presence of an IGrM more extended than the CGM of individual group members (see also Bordoloi et al. 2011; Bielby et al. 2017).

Our tomographic observations of cool ($\sim 10^4 \text{ K}$) gas in the field of SGAS J0033+02 provide a unique opportunity to probe the IGrM from within, at smaller impact parameters than those accessible through quasar sightlines. As shown in the left panel of Fig. 3, the ARCTOMO measurements, obtained at projected distances of less than one-fifth of the group’s virial radius, follow the trend reported by Cherrey et al. (2024). A joint fit to the *intervening* Mg II data from both the ARCTOMO and Cherrey et al. samples yields:

$$\log W_r^{2796} [\text{\AA}] = (-1.53 \pm 0.28) \times d_{\text{proj}}/R_{\text{vir}} + 0.70 \pm 0.22. \quad (2)$$

The low scatter observed across the inner group halo suggests a well-mixed IGrM, although this may also reflect the large ARCTOMO beams. The DtB Mg II absorption detected in front of G1 and G2 falls along this relation, indicating that these sightlines probe velocity dispersions consistent with those of intervening systems. At larger projected distances, beyond one-fifth of the virial radius, no Mg II absorption is detected from ARCTOMO, consistent with both the declining trend and our relatively loose upper limits.

Compared to field galaxies (Nielsen et al. 2013), galaxy groups exhibit enhanced Mg II absorption, implying that substantial amounts of cool gas have been displaced from galaxies into the IGrM through feedback processes. In the right panel of Fig. 3, we show the velocity ranges of gas clouds along each sightline, measured relative to the group’s mass-weighted systemic velocity. All measured velocities lie well below the group’s escape velocity, indicating that the cool gas is strongly gravitationally bound to the group.

6.2. Chemical enrichment

The chemical enrichment of the gas can be probed through the relative abundances of iron and magnesium at different locations across the field. In the case of SGAS J0033+02, most of the Fe II and Mg II absorption lines are strongly saturated, implying that their equivalent widths primarily trace the velocity dispersion of individual clouds along each sightline. Across all background sources, the (Fe/Mg) ratio remains consistent within the measurement uncertainties, except towards Ci2, where the Fe II lines are weaker (see Table 4). In this region, the ratio suggests a lower iron abundance relative to magnesium and/or a reduced metallicity. Since iron is predominantly produced by Type Ia supernovae on longer timescales than the alpha-elements like magnesium (produced in core-collapse supernovae), a lower Fe/Mg ratio indicates younger or less chemically evolved gas (e.g., Matteucci & Greggio 1986). Overall, the IGrM in the field of SGAS J0033+02 appears chemically homogeneous, with a possible decline in metallicity towards the outer

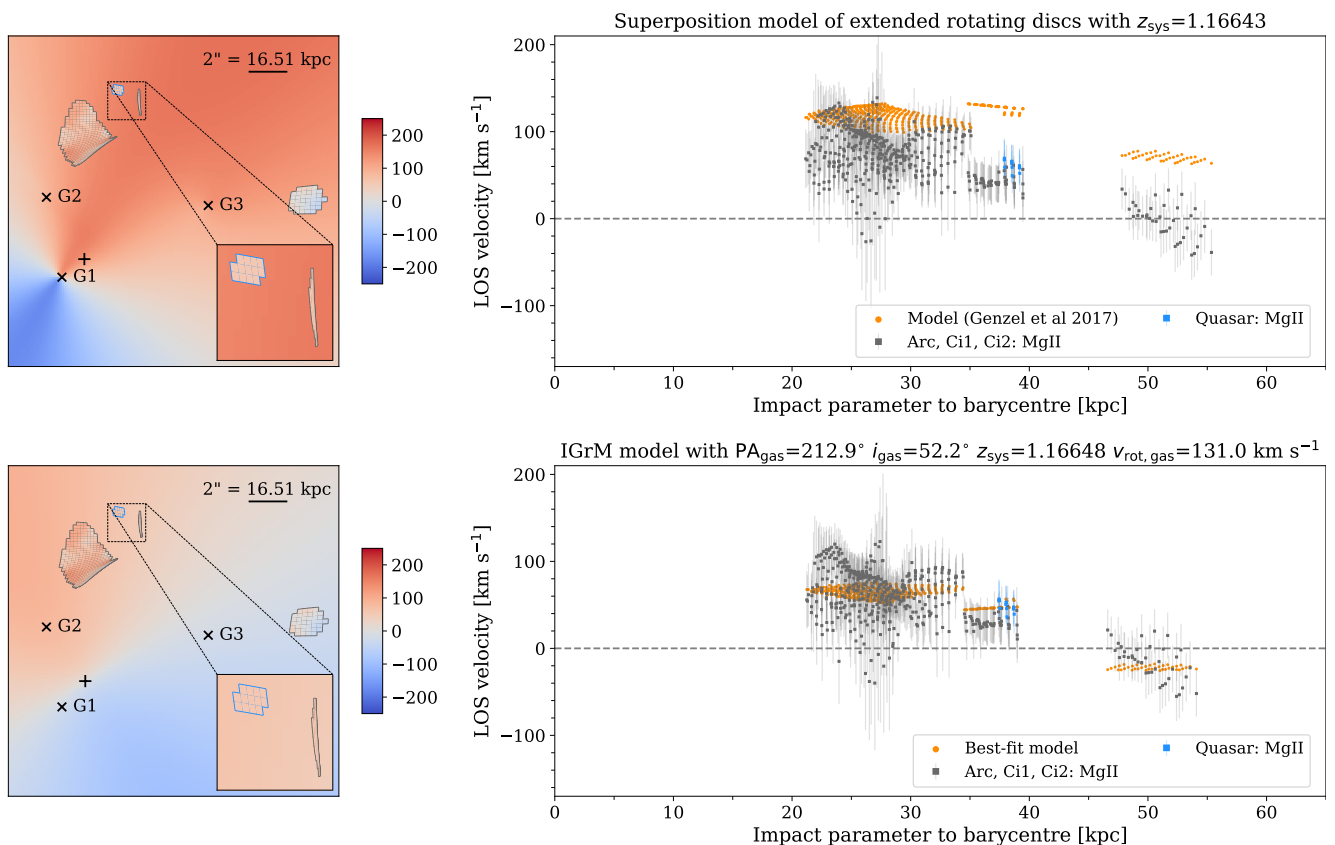


Fig. 4: Superposition model of extended rotating discs (*upper panels*) and rotating IGrM model (*lower panels*). *Left panels*: Modelled velocity maps with the observed intervening Mg II mean velocities overlaid for each of the four delensed sources. The inset shows the zoom-in on a region encompassing Ci1 and the quasar. *Right panels*: Model-predicted velocities (orange) at the positions of the Arc, Ci1, Ci2, and the quasar, as a function of impact parameter relative to the barycentre, marked by a plus sign in the left panels (superposition model: barycentre of G1 to G3; IGrM: G1 to G5). The observed Mg II velocities are displayed in black for the Arc, Ci1, and Ci2, and in blue for the quasar.

regions. This interpretation is consistent with the non-detection of Mg II beyond a projected distance of 65 kpc from the group’s barycentre.

6.3. Gas kinematics

The detected intervening Mg II absorption lies predominantly along the projected major axis of G1, making our non-down-the-barrel observations largely insensitive to star-formation-driven outflows, which are expected to occur along the minor axis. To investigate the origin of this absorption, we considered three scenarios: (1) extended gaseous discs associated with G1, G2, or G3; (2) a superposition of such discs; and (3) an IGrM halo shared by the group.

Using GalPak^{3D} modelling (see Sect. 4.3), we extrapolated the [O II] emission-line kinematics of each galaxy and compared the resulting velocity fields with the Mg II absorption. We adopted realistic rotation curves from Genzel et al. (2020), which account for the increasing velocity dispersion in the outer disc regions. We find that single-disc models fail to reproduce the mean absorption velocities with high confidence (see Fig. D.3), with reduced χ^2_v values of 17.7, 9.61, and 154 for G1, G2, and G3, respectively. This discrepancy is striking for G1, the most massive galaxy in the group, which should dominate the absorption. Similarly, G2’s kinematics alone do not match the observations, despite its close

projected distance to the Arc. Nevertheless, G2’s extrapolated velocity field shows better agreement with the Mg II absorption in front of the Arc than G1’s, offering clues to the gas origin. We then considered a superposition model by calculating the mass-weighted mean velocities from the extended disc models of G1, G2, and G3 across the field. This approach improves the match near the Arc ($\chi^2_v = 4.43$) but fails at larger distances (see Fig. 4, upper panels).² Overall, the Mg II gas exhibits kinematics more similar to those of the least massive galaxies than to G1’s. While this confirms some level of association with individual galaxies, it is weaker than anticipated. Indeed, the Mg II gas is confined to a narrow velocity range of $\sim \pm 50$ km s⁻¹ around the group’s systemic redshift, much smaller than the stellar rotational velocities. Furthermore, in the direction of Ci2, the gas counter-rotates relative to the ISM of both G1 and G2 (see Fig. D.3), challenging the validity of the superposition model beyond a first approximation.

² Note that the regions shown in Fig. 4 represent all spaxels where Mg II absorption is detected above our significance threshold ($S/N > 2$ in the continuum). The Arc appears more extended than in the lower panel of Fig. 2 because the spatial resolution of MUSE is lower than that of *HST*. Moreover, Ci1 appears narrow in both cases due to the geometry of the delensing transformation, which compresses this image along one dimension (east-west) in the absorber plane.

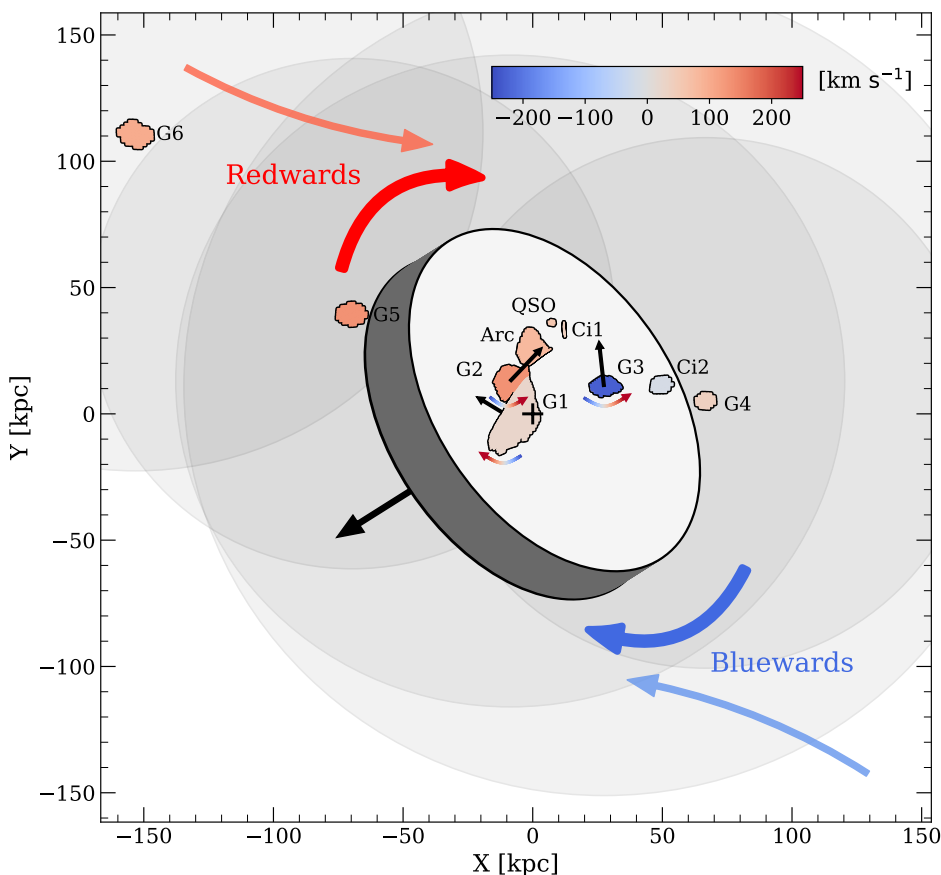


Fig. 5. Schematic of the orientation and kinematics of the intragroup medium in the compact galaxy group in the field of SGAS J0033+02. Each region is colour-coded based on the mean velocity offset of the observed Mg II (or [O II]) gas relative to the mass-weighted mean redshift of G1 to G5 ($z = 1.16648$). The axes (black arrows) and directions (blue and/or red arrows) of rotation of G1, G2, G3, and the intragroup medium are indicated. The shaded, overlapping circles denote the extent of one virial radius around each galaxy.

Table 5: Orientation-kinematic analysis of Mg II absorption.

Rotation centre	$PA_{\text{gas}}^{a,b}$ [$^{\circ}$]	i_{gas}^a [$^{\circ}$]	z_{sys}^c	$v_{\text{rot,gas}}^{a,d}$ [km s^{-1}]	χ_v^{2e}
G1	231_{-2}^{+1}	42_{-13}^{+10}	1.16666	150_{-13}^{+36}	0.711
G1+G2	238_{-1}^{+1}	40_{-12}^{+13}	1.16674	151_{-17}^{+45}	0.713
G1→G3	209_{-2}^{+2}	57_{-8}^{+5}	1.16643	134_{-5}^{+7}	0.734
G1→G5	213_{-2}^{+2}	52_{-18}^{+7}	1.16648	131_{-6}^{+29}	0.729

Notes. ^(a) Delensed absorber plane; ^(b) Position angle of the approaching semi-major axis (east of north); ^(c) Mass-weighted mean redshift of the considered galaxies; ^(d) Assuming a rotation curve $v(r) = v_{\text{rot,gas}} \frac{2}{\pi} \arctan(r/r_i)$; ^(e) Reduced Chi-squared.

Motivated by these results, we examined a model in which the gas resides in a thick, rotating layer or flattened spheroidal halo. Using the Mg II velocities observed towards the Arc, Ci1, Ci2, and the quasar, we applied Markov Chain Monte Carlo (MCMC) modelling with Bayesian inference to sample the posterior distributions of position angle, inclination, and rotational velocity within the following ranges: $PA_{\text{gas}} = [0; 360]^{\circ}$, $i_{\text{gas}} = [0; 90]^{\circ}$, and $v_{\text{rot,gas}} = [0; 300] \text{ km s}^{-1}$. The rotation centre and systemic redshift were allowed to differ from those of G1, considering instead the barycentres of the two, three, or five most massive group members. In each case, the systemic redshift was fixed to the mass-weighted mean of the selected galaxies. A range of vertical scale heights was also explored but found to have negligible impact on the fits and to remain unconstrained. The best-fitting parameters are listed in Table 5, and the model based on the barycentre and combined redshift of G1, G2,

and G3 is shown in Fig. 4 (lower panels). All tested rotation centres yield consistent results, indicating that the derived parameters are robust to this choice. This supports the presence, in addition to individual galaxy discs, of an IGrM phase with a projected rotational velocity of $v_{\text{rot,gas}} \sin i \approx 103 \text{ km s}^{-1}$. Interestingly, the inferred rotation direction of the halo aligns with the orbital motions of all six group galaxies (see Fig. 5), suggesting that angular momentum is acquired through infall along nearby large-scale structure filaments and subsequent mixing with metal-enriched gas. The model also reproduces the relative velocity between G1 and G2 ($\approx -94 \text{ km s}^{-1}$), implying that G2 is receding from G1. If G1 and G2 have previously interacted, G2 is now located behind G1. The spin of G1 is oriented towards G5 and G6, consistent with filamentary accretion scenarios (e.g., Welker et al. 2018), whereas the misalignment of the spin axes of G1, G2, and G3 indicates previous interactions.

Intervening Mg II absorption probes the entire halo, whereas gas detected in front of individual galaxies carries the signature of their own ISM and CGM. This is particularly evident for G3, whose DtB absorption exhibits substantial velocity dispersion (see Table 4 and Fig. C.2). Towards both G1 and G2, the gas is blueshifted by $\approx -40 \text{ km s}^{-1}$ relative to the halo model, reflecting the influence of stellar winds and/or AGN-driven outflows not included in the model. Nevertheless, the relative velocity between these two components ($\approx +40 \text{ km s}^{-1}$) is well reproduced in both magnitude and rotation direction, providing further support for the rotating IGrM scenario, as illustrated in Fig. 5. Each spatially resolved background source (the Arc, Ci1, and Ci2; see lower right panel of Fig. 4) also

exhibits internal velocity scatter exceeding that expected from pure rotation, indicating the presence of turbulence and localised gas motions within the IGrM.

6.4. Total gas mass

From the observed Mg II gas kinematics, we can estimate the dynamical mass of the system and constrain its total (cool+warm+hot) baryonic gas mass. To do this, we applied the virial theorem, which describes the balance between gravitational, centrifugal, and pressure forces for a system at equilibrium. Under this assumption, the dynamical mass enclosed within a rotating mass distribution of radius R can be written as (e.g., [Epinat et al. 2009](#); [Wolf et al. 2010](#)):

$$M_{\text{dyn}}(r < R) [M_{\odot}] = 2.33 \times 10^5 (v_{\text{rot}}^2 + 3 \sigma_v^2) R, \quad (3)$$

where v_{rot} is the rotational velocity (in km s^{-1}), σ_v is the line-of-sight velocity dispersion (in km s^{-1}), and R is the radius of the mass distribution perpendicular to the rotation axis (in kpc).

Strong Mg II absorption in the field of SGAS J0033+02 is observed out to the projected distance of Ci2. For this reason, we considered the mass enclosed within a radius of 85 kpc, which is the deprojected distance between Ci2 and the group's barycentre. Using the observed mean velocity dispersion of 122 km s^{-1} and a rotational velocity of 131 km s^{-1} (see Sects. 5.1 and 6.3), we infer a total dynamical mass of $1.22 \times 10^{12} M_{\odot}$. For comparison, the combined stellar and ISM masses of G1, G2, and G3, enclosed within this radius, amount to $1.52 \times 10^{11} M_{\odot}$. From dark matter theory (e.g., [Navarro et al. 1997](#)), the dark matter-to-total mass fraction at a radius of 85 kpc for a halo mass of $1.32 \times 10^{13} M_{\odot}$ lies in the range 0.67 – 0.77, depending on the assumed parameters. This implies a total baryonic (cool+warm+hot) gas mass of $1.3\text{--}2.5 \times 10^{11} M_{\odot}$, corresponding to approximately 55% of all baryons within one-quarter of the group's virial radius. When rescaled to the number of galaxies, this corresponds to a total gas mass per galaxy of $6.3 \times 10^{10} M_{\odot}$ for a stellar mass of $5 \times 10^{10} M_{\odot}$.

The calculation assumes the IGrM gas is in dynamical equilibrium, which may not be strictly valid in this actively star-forming and interacting galaxy group. However, several lines of evidence support this approximation: (1) the coherent velocity field observed across ≥ 60 kpc scales suggests organized rather than chaotic motions; (2) all measured gas velocities lie well below the group escape velocity (see Fig. 3, right panel), indicating gravitationally bound gas; and (3) the group's dynamical time (crossing time) at $R \sim 85$ kpc is $\tau_{\text{dyn}} \sim R/v_{\text{rot}} \sim 0.65$ Gyr, sufficient for at least partial relaxation. The virial theorem has been widely applied to estimate masses of galaxy groups and clusters from kinematic data (e.g., [Rines & Diaferio 2006](#); [Epinat et al. 2009](#)). Nevertheless, ongoing interactions, turbulence, and/or magnetic pressure support likely introduce systematic uncertainties of order 50% in our mass estimates.

From analytical modelling, [Berg et al. \(2025\)](#) estimated the cool gas mass towards the extended background sources of SGAS J0033+02 and derived a value of $1.2 \times 10^9 M_{\odot}$ over an area of 350 kpc^2 . Within the framework of a rotating IGrM, extrapolating this mass to a radius of 85 kpc yields a cool gas mass of $7.8 \times 10^{10} \times C_f M_{\odot}$, where C_f is the gas covering fraction. Compared to our constrained total gas mass, this implies, for cool-gas covering fractions $C_f \gtrsim 0.5$,

a cool phase accounting for at least 20% of the total gas mass within one-quarter of the group's virial radius, the rest corresponding to warm+hot gas.

These results are consistent with previous estimates of the CGM gas mass around sub- L^* to L^* galaxies, as inferred from both observations and cosmological simulations (e.g., [Werk et al. 2014](#); [Stern et al. 2016](#); [Prochaska et al. 2017](#); [Nelson et al. 2020](#); [Faerman & Werk 2023](#); [Wright et al. 2024](#)). However, unlike isolated galaxies, the CGM of the individual galaxies in the compact group in the field of SGAS J0033+02 appears to overlap, leading to the existence of a pervasive IGrM with its own kinematic behaviour (see Sect. 6.3). Based on the coherence of the observed velocity field and the angular momentum it carries, we suggest that the cool gas in the IGrM is kinematically locked within a warm-hot halo phase rather than reaccreting onto the parent galaxies. The lack of reaccretion of the gas may lead to the rapid quenching of star formation, over less than 500 Myr (e.g., [Bitsakis et al. 2016](#); [Skarbinski et al. 2025](#)), particularly in lower mass galaxies like G2.

7. Conclusions

Gravitational-arc tomography provides a complementary approach to quasar absorption-line studies, which probe multiphase gas in the CGM ([Tumlinson et al. 2011](#); [Werk et al. 2014](#)). [Chen et al. \(2010\)](#) found that Mg II absorbers with $W_r^{2796} > 0.1 \text{ \AA}$ exhibit covering fractions of approximately 80% within 100 kpc of galaxies with luminosities $L \leq L^*$. Similarly, [Neeleman et al. \(2016\)](#) showed that a substantial fraction of molecular gas detected in absorption originates from the CGM rather than the disc of an isolated galaxy at $z \simeq 0.1$. Studies of galaxy groups indicate that absorption often arises from multiple galaxies ([Bielby et al. 2017](#); [Fossati et al. 2019](#); [Dutta et al. 2020, 2021](#)). While superposition models ([Nielsen et al. 2018](#); [Bordoloi et al. 2011](#); [Fossati et al. 2019](#)) typically reproduce the equivalent widths, we have shown that they do not capture the kinematics of absorption in a compact group, highlighting their limitations in describing the IGrM. Unlike previous ARCTOMO studies, which primarily targeted isolated galaxies ([Lopez et al. 2018, 2020](#); [Tejos et al. 2021](#)), the present work reveals the complexity of gas dynamics in group environments (see also [Cherrey et al. 2024](#); [Fernández-Figueroa et al. 2024](#)).

Firstly, our results demonstrate that the IGrM around star-forming galaxies in groups is abundant in cool gas and metals. The ubiquity and spatial coherence of the IGrM in the compact group in the field of SGAS J0033+02 suggest efficient gas processing and mixing. Although G1 was initially selected based on prior Mg II absorption against the Arc, integral-field spectroscopy of all sources across the field revealed a far greater extent and coverage of cool gas than anticipated. While cool gas is typically expected near star-forming regions and galactic discs, our observations reveal gas escaping in front of G1 and G2, implying metal enrichment of the halo. Moreover, the presence of cool gas at large distances, distributed across the field, indicates that the stripping of dwarf galaxies, in addition to star-formation-driven winds, plays a significant role in redistributing metals. This aligns with [Nielsen et al. \(2022\)](#), who reported a compact galaxy group giving rise to a DLA with ultra-strong Mg II absorption at $z \simeq 2.4$, and with [Puglisi et al.](#)

(2021), who observed ISM material stripped by tidal forces in a galaxy merger at $z \approx 1.4$.

We find evidence for a multiphase IGrM that contributes substantially to the Mg II absorption signal as well as exhibits coherent large-scale rotational motions. While previous observations have hinted at coherent motions in the IGrM (e.g., [Leclercq et al. 2022](#)), we observe, for the first time, coherent 2D kinematics of intervening absorption up to a deprojected distance of ~ 85 kpc, encompassing the primary group galaxies and, most importantly, rotating with them. Applying the virial theorem, we constrain the total baryonic (cool+warm+hot) gas mass to $\sim 2 \times 10^{11} M_{\odot}$ within one-quarter of the group's virial radius, with the cool phase accounting for at least 20% of this total. Substantial amounts of cool gas suggest ongoing growth of cool clouds within a hot halo. This process involves interaction of cool ($\sim 10^4$ K) clouds with warm and hot gas along their trajectories and adiabatic compression, with long dissipation timescales ([Kanjilal et al. 2021](#); [Gronke & Oh 2018](#); [Gronke et al. 2022](#)).

Simulations predict that extended multiphase gas with sub-escape velocities condenses near the wakes of satellite galaxies and intergalactic filaments on scales approaching the halo virial radius ([Nelson et al. 2020](#)). The large-scale coherence of gas kinematics observed here supports a picture in which metal-enriched gas is locked in a rotating halo phase, acquiring angular momentum and mixing with gas at the intersection of infalling filaments, as predicted by cosmological simulations (e.g., [Stern et al. 2024](#)). Our results suggest angular momentum organization across cosmic scales, from isolated galaxy spins aligned with individual filaments (e.g., [Welker et al. 2018](#); [Kraljic et al. 2021](#); [Tudorache et al. 2025](#)) to coherent group-scale rotation at their intersection. Consequently, intervening absorbers may not always be associated with individual galaxies, particularly in massive halos (e.g., [Weng et al. 2023](#)). Instead, high-redshift strong Mg II absorbers may trace shared, metal-enriched halos shaped by galaxy interactions and feedback, with stripped and outflowing gas accumulating in the IGrM over time.

Acknowledgements. We are grateful to Andrea Afruni and Rongmon Bordoloi for insightful discussions. CL acknowledges support from ESO during his research period. FM and FB acknowledge funding from ANID through Becas/Magister Nacional 22240417, Basal project FB210003, FONDECYT grant 1230231, and support from CATA and ESO. NT acknowledges support from FONDECYT grant 1231187. This work is based on observational data collected by the ARCTOMO collaboration (<https://sites.google.com/view/arctomo/home>).

References

Afruni, A., Lopez, S., Anshul, P., et al. 2023, *A&A*, 680, A112
 Atek, H., Kneib, J.-P., Pacifici, C., et al. 2014, *ApJ*, 789, 96
 Bacon, R., Accardo, M., Adjali, L., et al. 2010, in *Society of Photo-Optical Instrumentation Engineers (SPIE) Conference Series*, Vol. 7735, *Ground-based and Airborne Instrumentation for Astronomy III*, ed. I. S. McLean, S. K. Ramsay, & H. Takami, 773508
 Bacon, R., Brinchmann, J., Conseil, S., et al. 2023, *A&A*, 670, A4
 Barbary, K. 2018, *SEP: Source Extraction and Photometry*, *Astrophysics Source Code Library*, record ascl:1811.004
 Bauer, A. E., Drory, N., Hill, G. J., & Feulner, G. 2005, *ApJ*, 621, L89
 Behroozi, P. S., Wechsler, R. H., & Conroy, C. 2013, *ApJ*, 770, 57
 Berg, T. A. M., Afruni, A., Ledoux, C., et al. 2025, *A&A*, 693, A200
 Bertin, E. & Arnouts, S. 1996, *A&AS*, 117, 393
 Bielby, R., Crighton, N. H. M., Fumagalli, M., et al. 2017, *MNRAS*, 468, 1373

Bitsakis, T., Dultzin, D., Ciesla, L., et al. 2016, *MNRAS*, 459, 957
 Bordoloi, R., Lilly, S. J., Knobel, C., et al. 2011, *ApJ*, 743, 10
 Bordoloi, R., O'Meara, J. M., Sharon, K., et al. 2022, *Nature*, 606, 59
 Bouché, N., Carfantan, H., Schroetter, I., Michel-Dansac, L., & Contini, T. 2015, *AJ*, 150, 92
 Bruzual, G. & Charlot, S. 2003, *MNRAS*, 344, 1000
 Calzetti, D., Armus, L., Bohlin, R. C., et al. 2000, *ApJ*, 533, 682
 Carnall, A. C., McLure, R. J., Dunlop, J. S., et al. 2019, *MNRAS*, 490, 417
 Carnall, A. C., McLure, R. J., Dunlop, J. S., & Davé, R. 2018, *MNRAS*, 480, 4379
 Chabanier, S., Etourneau, T., Le Goff, J.-M., et al. 2022, *ApJS*, 258, 18
 Chen, H.-W., Helsby, J. E., Gauthier, J.-R., et al. 2010, *ApJ*, 714, 1521
 Cherrey, M., Bouché, N. F., Zabl, J., et al. 2024, *MNRAS*, 528, 481
 Davies, L. J. M., Driver, S. P., Robotham, A. S. G., et al. 2016, *MNRAS*, 461, 458
 DeFelippis, D., Bouché, N. F., Genel, S., et al. 2021, *ApJ*, 923, 56
 DeFelippis, D., Genel, S., Bryan, G. L., et al. 2020, *ApJ*, 895, 17
 Dutta, R., Fumagalli, M., Fossati, M., et al. 2021, *MNRAS*, 508, 4573
 Dutta, R., Fumagalli, M., Fossati, M., et al. 2020, *MNRAS*, 499, 5022
 Elmegreen, D. M., Elmegreen, B. G., Marcus, M. T., et al. 2009, *ApJ*, 701, 306
 Epinat, B., Contini, T., Le Fèvre, O., et al. 2009, *A&A*, 504, 789
 ESO CPL Development Team. 2015, *EsoRex: ESO Recipe Execution Tool*, *Astrophysics Source Code Library*
 Faerman, Y. & Werk, J. K. 2023, *ApJ*, 956, 92
 Faucher-Giguère, C.-A. & Oh, S. P. 2023, *ARA&A*, 61, 131
 Fernández-Figueroa, A., Kacprzak, G. G., Nielsen, N. M., et al. 2024, *MNRAS*, 531, 3658
 Fernández-Figueroa, A., Lopez, S., Tejos, N., et al. 2022, *MNRAS*, 517, 2214
 Fischer, T. C., Rigby, J. R., Mahler, G., et al. 2019, *ApJ*, 875, 102
 Fossati, M., Fumagalli, M., Lofthouse, E. K., et al. 2019, *MNRAS*, 490, 1451
 Gaia Collaboration, Vallenari, A., Brown, A. G. A., et al. 2023, *A&A*, 674, A1
 Gauthier, J.-R. 2013, *MNRAS*, 432, 1444
 Genzel, R., Price, S. H., Übler, H., et al. 2020, *ApJ*, 902, 98
 Ginsburg, A., Sokolov, V., de Val-Borro, M., et al. 2022, *AJ*, 163, 291
 Gronke, M. & Oh, S. P. 2018, *MNRAS*, 480, L111
 Gronke, M., Oh, S. P., Ji, S., & Norman, C. 2022, *MNRAS*, 511, 859
 Guha, L. K., Srianand, R., & Petitjean, P. 2024, *MNRAS*, 527, 5075
 Hinton, S. R., Davis, T. M., Lidman, C., Glazebrook, K., & Lewis, G. F. 2016, *Astronomy and Computing*, 15, 61
 Huang, Y.-H., Chen, H.-W., Shectman, S. A., et al. 2021, *MNRAS*, 502, 4743
 Joshi, B. A., Appleton, P. N., Blanc, G. A., et al. 2019, *ApJ*, 878, 161
 Jullo, E., Kneib, J. P., Limousin, M., et al. 2007, *New Journal of Physics*, 9, 447
 Kanjilal, V., Dutta, A., & Sharma, P. 2021, *MNRAS*, 501, 1143
 Kennicutt, R. C. & Evans, N. J. 2012, *ARA&A*, 50, 531
 Kraljic, K., Duckworth, C., Tojeiro, R., et al. 2021, *MNRAS*, 504, 4626
 Krogager, J. K., Fynbo, J. P. U., Møller, P., et al. 2012, *MNRAS*, 424, L1
 Kroupa, P. 2001, *MNRAS*, 322, 231
 Lara-López, M. A., Hopkins, A. M., López-Sánchez, A. R., et al. 2013, *MNRAS*, 434, 451
 Leclercq, F., Verhamme, A., Epinat, B., et al. 2022, *A&A*, 663, A11
 Ledoux, C., Petitjean, P., & Srianand, R. 2003, *MNRAS*, 346, 209
 Lopez, S., Tejos, N., Barrientos, L. F., et al. 2020, *MNRAS*, 491, 4442
 Lopez, S., Tejos, N., Ledoux, C., et al. 2018, *Nature*, 554, 493
 Matteucci, F. & Greggio, L. 1986, *A&A*, 154, 279
 Mortensen, K., Keerthi Vasan, G. C., Jones, T., et al. 2021, *ApJ*, 914, 92
 Moster, B. P., Somerville, R. S., Maulbetsch, C., et al. 2010, *ApJ*, 710, 903
 Muzahid, S., Srianand, R., & Charlton, J. 2015, *MNRAS*, 448, 2840
 Navarro, J. F., Frenk, C. S., & White, S. D. M. 1997, *ApJ*, 490, 493
 Neeleman, M., Kanekar, N., Prochaska, J. X., Rafelski, M. A., & Kahinga, L. A. 2025, *ApJ*, 983, 26
 Neeleman, M., Prochaska, J. X., Zwaan, M. A., et al. 2016, *ApJ*, 820, L39
 Nelson, D., Sharma, P., Pillepich, A., et al. 2020, *MNRAS*, 498, 2391
 Nestor, D. B., Johnson, B. D., Wild, V., et al. 2011, *MNRAS*, 412, 1559
 Nestor, D. B., Turnshek, D. A., Rao, S. M., & Quider, A. M. 2007, *ApJ*, 658, 185

- Nielsen, N. M., Churchill, C. W., & Kacprzak, G. G. 2013, *ApJ*, 776, 115
- Nielsen, N. M., Kacprzak, G. G., Pointon, S. K., Churchill, C. W., & Murphy, M. T. 2018, *ApJ*, 869, 153
- Nielsen, N. M., Kacprzak, G. G., Pointon, S. K., et al. 2020, *ApJ*, 904, 164
- Nielsen, N. M., Kacprzak, G. G., Sameer, et al. 2022, *MNRAS*, 514, 6074
- Noterdaeme, P., Ledoux, C., Petitjean, P., & Srianand, R. 2008, *A&A*, 481, 327
- Noterdaeme, P., Petitjean, P., Ledoux, C., & Srianand, R. 2009, *A&A*, 505, 1087
- Pearson, W. J., Wang, L., Hurley, P. D., et al. 2018, *A&A*, 615, A146
- Péroux, C. & Howk, J. C. 2020, *ARA&A*, 58, 363
- Pessa, I., Tejos, N., & Moya, C. 2020, in *Astronomical Society of the Pacific Conference Series*, Vol. 522, *Astronomical Data Analysis Software and Systems XXVII*, ed. P. Ballester, J. Ibsen, M. Solar, & K. Shorridge, 61
- Piqueras, L., Conseil, S., Shepherd, M., et al. 2019, in *Astronomical Society of the Pacific Conference Series*, Vol. 521, *Astronomical Data Analysis Software and Systems XXVI*, ed. M. Molinaro, K. Shorridge, & F. Pasian, 545
- Prochaska, J. X., Werk, J. K., Worseck, G., et al. 2017, *ApJ*, 837, 169
- Puglisi, A., Daddi, E., Brusa, M., et al. 2021, *Nature Astronomy*, 5, 319
- Puschnig, J., Hayes, M., Agertz, O., et al. 2023, *MNRAS*, 524, 3913
- Rigby, J. R., Bayliss, M. B., Sharon, K., et al. 2018, *AJ*, 155, 104
- Rines, K. & Diaferio, A. 2006, *AJ*, 132, 1275
- Rubin, K. H. R., Prochaska, J. X., Koo, D. C., Phillips, A. C., & Weiner, B. J. 2010, *ApJ*, 712, 574
- Sanders, R. L., Shapley, A. E., Jones, T., et al. 2021, *ApJ*, 914, 19
- Schlafly, E. F. & Finkbeiner, D. P. 2011, *ApJ*, 737, 103
- Skarbinski, M., Rowlands, K., Alatalo, K., et al. 2025, *arXiv e-prints*, arXiv:2509.18278
- Smith, B. J., Giroux, M. L., Struck, C., & Hancock, M. 2010, *AJ*, 139, 1212
- Solimano, M., González-López, J., Barrientos, L. F., et al. 2021, *A&A*, 655, A42
- Soto, K. T., Lilly, S. J., Bacon, R., Richard, J., & Conseil, S. 2016, *MNRAS*, 458, 3210
- Sparre, M., Whittingham, J., Damle, M., et al. 2022, *MNRAS*, 509, 2720
- Stern, J., Fielding, D., Hafen, Z., et al. 2024, *MNRAS*, 530, 1711
- Stern, J., Hennawi, J. F., Prochaska, J. X., & Werk, J. K. 2016, *ApJ*, 830, 87
- Tejos, N., López, S., Ledoux, C., et al. 2021, *MNRAS*, 507, 663
- Tudorache, M. N., Jung, S. L., Jarvis, M. J., et al. 2025, *MNRAS*, 544, 4306
- Tumlinson, J., Peeples, M. S., & Werk, J. K. 2017, *ARA&A*, 55, 389
- Tumlinson, J., Thom, C., Werk, J. K., et al. 2011, *Science*, 334, 948
- Weilbacher, P. M., Palsa, R., Streicher, O., et al. 2020, *A&A*, 641, A28
- Welker, C., Dubois, Y., Pichon, C., Devriendt, J., & Chisari, N. E. 2018, *A&A*, 613, A4
- Weng, S., Péroux, C., Karki, A., et al. 2023, *MNRAS*, 523, 676
- Werk, J. K., Prochaska, J. X., Tumlinson, J., et al. 2014, *ApJ*, 792, 8
- Wolf, J., Martinez, G. D., Bullock, J. S., et al. 2010, *MNRAS*, 406, 1220
- Wright, R. J., Somerville, R. S., Lagos, C. d. P., et al. 2024, *MNRAS*, 532, 3417

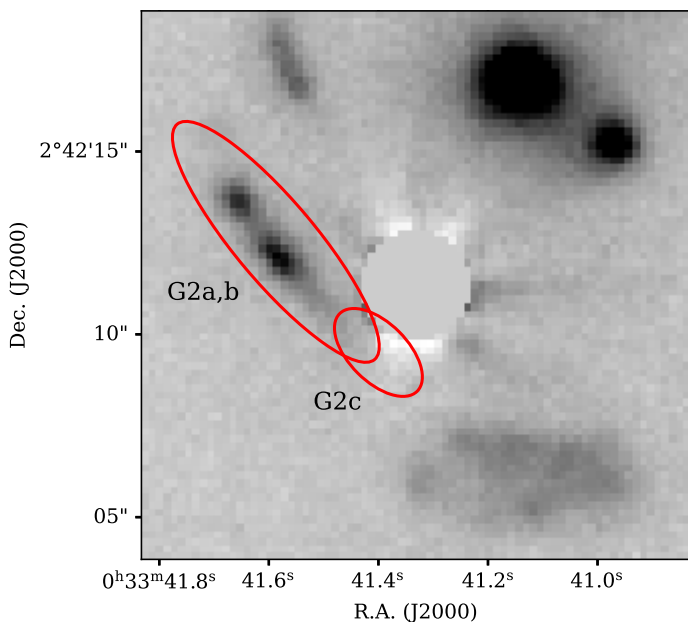


Fig. A.1: PSF subtraction and aperture masking of the Galactic star located between G1 (southwest) and G2 (east) in a MUSE narrow-band image centred on [O II] emission at $z = 1.17$. Light in this image may also arise from continuum emission. G2a and G2b refer to the brightest knots within G2. G2c denotes the region of G2 nearest to the stellar core (masked out) where [O II] emission can be detected.

Appendix A: Galactic foreground contamination

A bright Galactic star located near the centre of the field (see Fig. 1) is posing a challenge for the study of the region between G1 and G2 due to light contamination. This star, catalogued as GAIA DR3 2553567450013494784, is a K2V-type star with a mean G-band magnitude of 14.8 (Gaia Collaboration et al. 2023). To mitigate its impact on our targets, we adopted the following procedure. First, we modelled the point spread function (PSF) using three faint stars located in uncrowded regions of the MUSE white-light image, fitting 2D Moffat profiles. The resulting fits were consistent with one another, yielding best-fit parameters of FWHM = $0''.86$ at 8000 \AA and $\beta = 2.14$, in agreement with the results of Bacon et al. (2023).

Given its brightness, the central star exhibits artefacts caused by internal reflections and flat-fielding errors, which are apparent in the MUSE white-light image. For this reason, we focused on a narrow-band image centred on the [O II] emission lines of interest (see Sect. 3.1). We masked the stellar core using a circular aperture with a radius of eight spaxels, then fitted a 2D Moffat profile to the outer regions. This model was subtracted from the original image to produce a corrected version. While this method improved the representation of the annular region beyond an angular separation of $1''.6$ from the stellar core, residuals persisted in the innermost region. Consequently, this central region was masked and excluded from further analysis.

Fig. A.1 shows the residuals around the star after PSF subtraction and aperture masking. This cleaned image was used to measure star-formation rates based on [O II] emission (see Sect. 4.2).

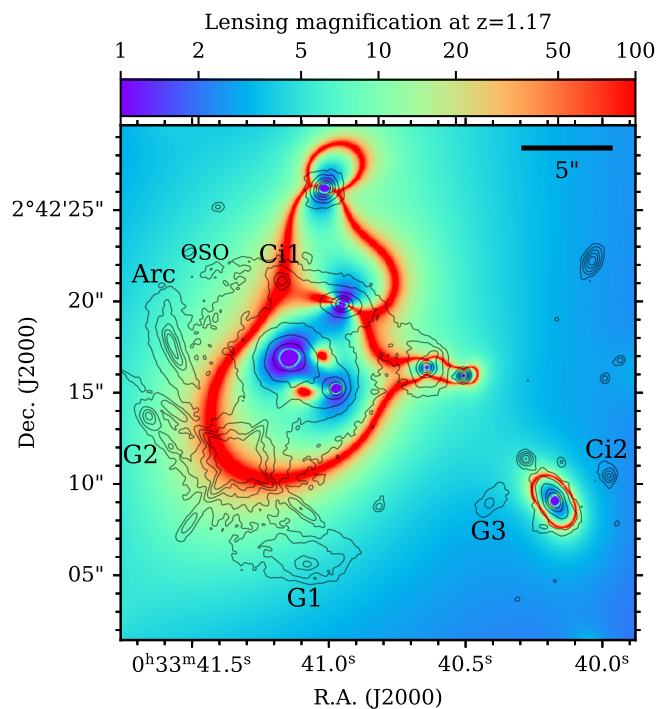


Fig. B.1: Magnification map of sources at $z = 1.17$, with critical lines highlighted in red. Black contours represent the *HST*/F140W image, overlaid to show the magnification of G1, G2, and G3, which are located at the same redshift as the detected Mg II absorption.

Appendix B: Magnification map

In this appendix, we present the magnification map of the lensing model (see Fig. B.1).

Appendix C: Emission and absorption lines

Nebular [O II] emission and Mg II and Mg I absorption lines detected at $z \approx 1.17$ in the integrated MUSE spectra are shown in Figs. C.1 and C.2 respectively.

Appendix D: Intensity and velocity maps

To derive an accurate representation of the data, we used the MUSE datacube to extract spatially-resolved information across the field at the redshift of the absorbing galaxy group. We employed a method similar to the one described in Berg et al. (2025) but with notable exceptions. We utilised the MUSE Python Data Analysis Framework, MPDAF (Piqueras et al. 2019), and first applied Gaussian resampling to the datacube in the spatial direction with $\sigma = 1.7$ spaxel, matching the seeing conditions during the observations ($\text{FWHM}_{\text{IQ}} \approx 0''.8$). This way, the information contained in each spaxel and the S/N ratio is optimised while preserving the native spatial resolution of the dataset. Each object of interest – G1, G2, G3, the Arc, Ci1, Ci2, and the quasar – were singled out in the image plane using elliptical apertures tailored to this resampled datacube, analogue to the method we employed to analyse the *HST* images (see Fig. 2). In addition, the central glare of the Galactic star, extending to a minimum diameter of $1''.4$,

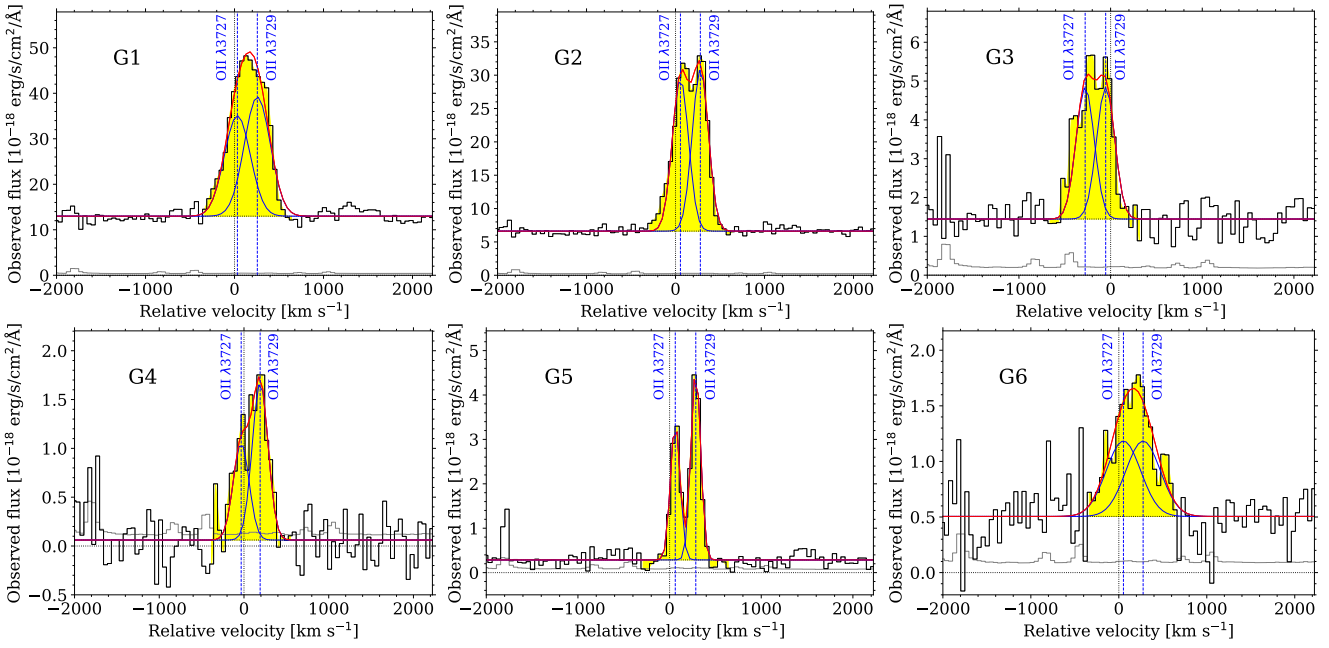


Fig. C.1: Nebular [O II] emission in individual galaxies, with binned fluxes and 1σ uncertainties shown in black and grey, emission lines in yellow, and double-Gaussian fits in red and blue. The zero point of the velocity scale corresponds to $z = 1.167$.

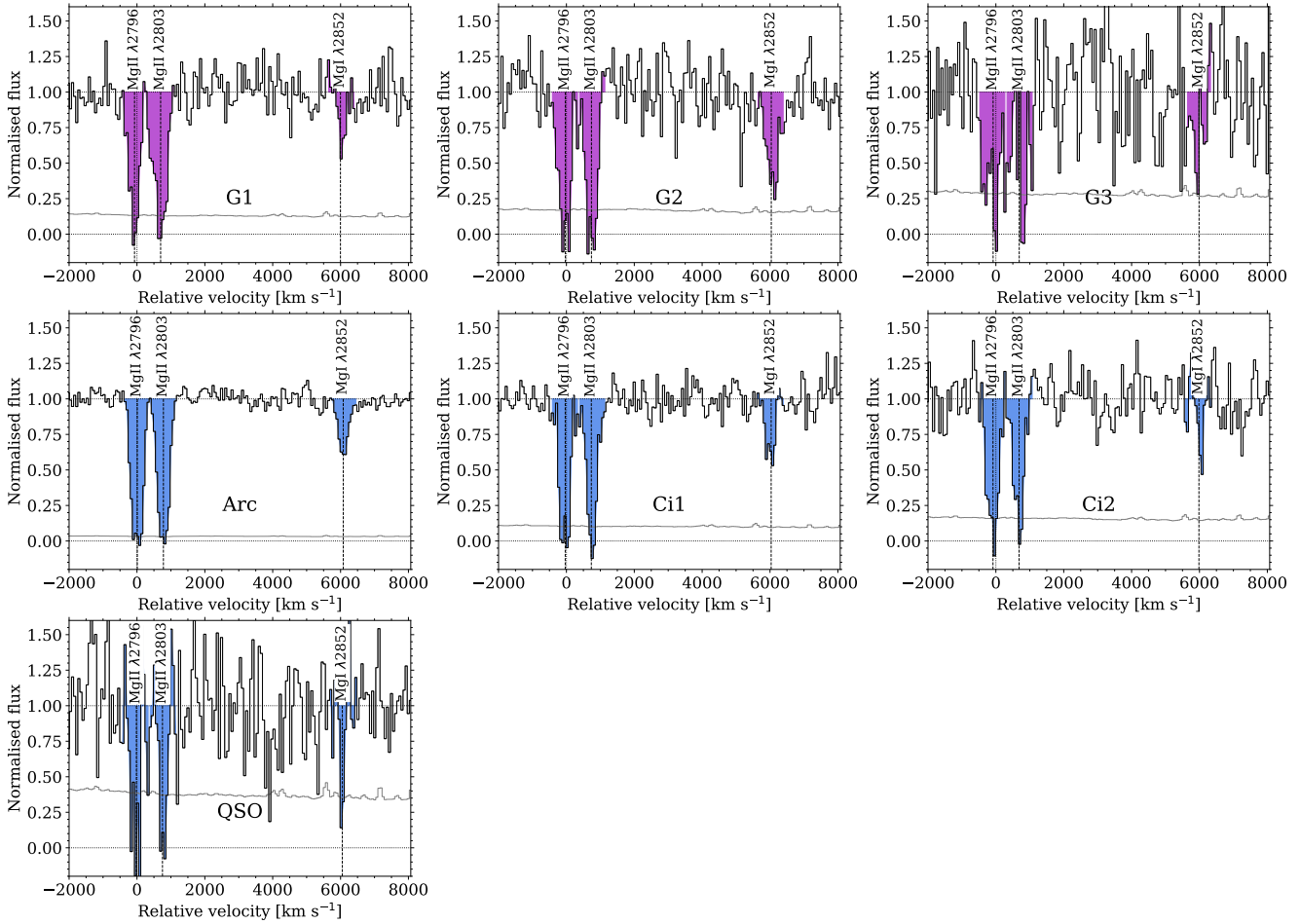


Fig. C.2: Down-the-barrel Mg I and Mg II absorption towards G1, G2, and G3 (top panels), and intervening absorption towards the Arc, Ci1, Ci2, and the quasar (middle and bottom panels). Normalised binned fluxes and 1σ uncertainties are shown in black and grey, with absorption lines filled in purple (top) or blue (middle and bottom). The zero point of the velocity scale corresponds to $z = 1.167$.

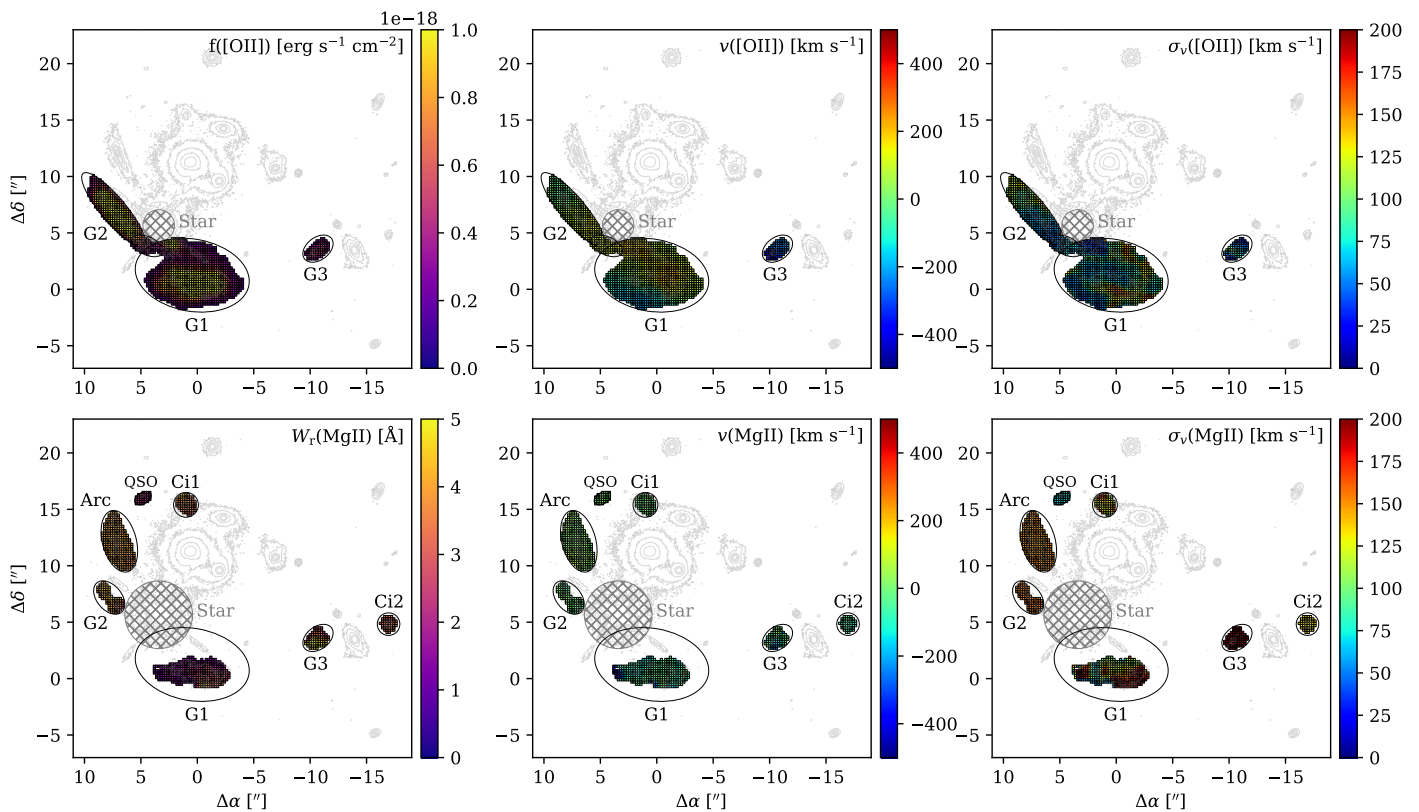


Fig. D.1: Maps of line fluxes (or equivalent widths), line-of-sight velocities, and velocity dispersion of the nebular [OII] emission (top panels) and MgII absorption (bottom panels) near the group centre, in the image plane. The orientation is north up and east to the left. The colour bar on the right-hand side of the plots indicates the measured quantity in the units specified in the inset. The zero point of the velocity scale corresponds to $z = 1.167$.

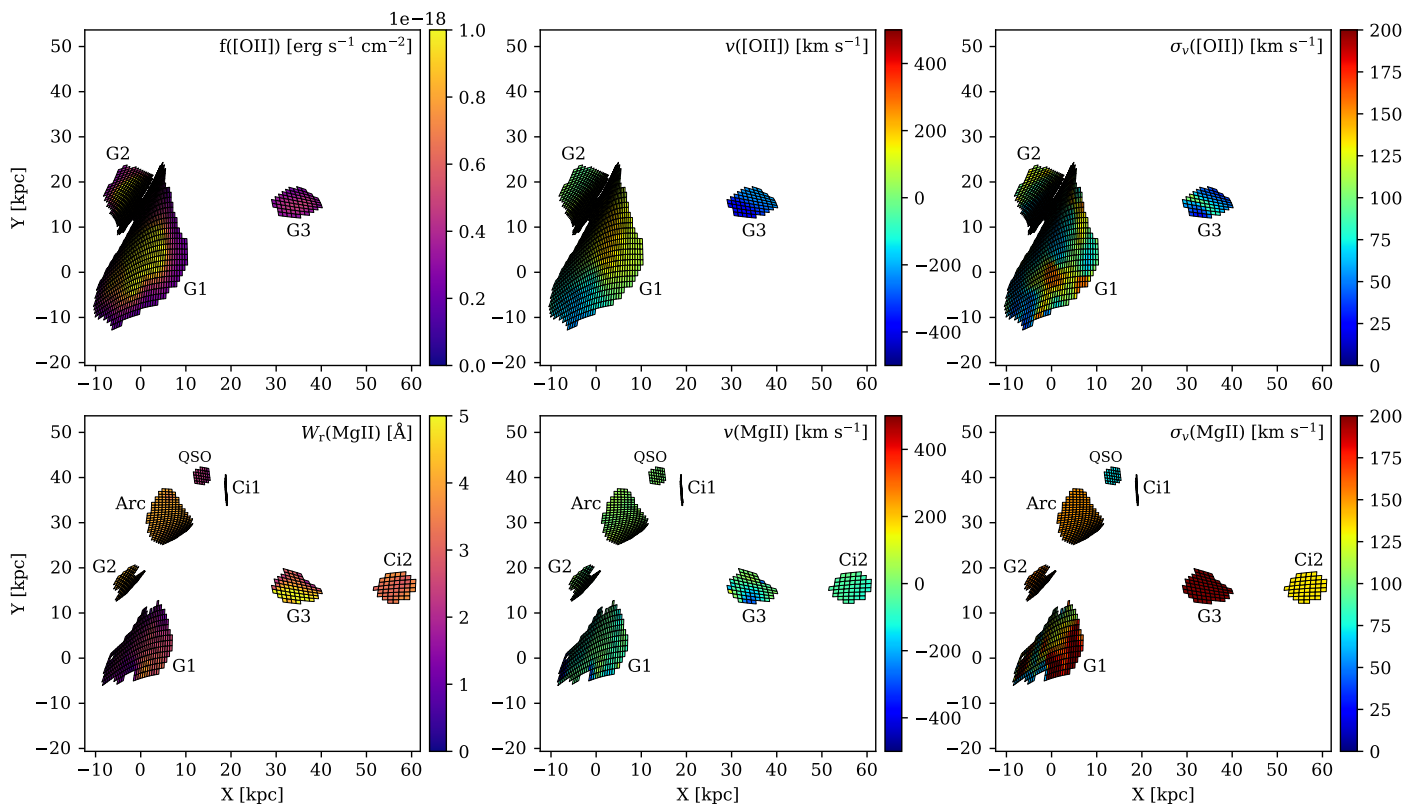


Fig. D.2: Same as Fig. D.1, but in the delensed absorber plane.

prevents any useful information about [O II] and Mg II to be extracted, even after subtraction of the stellar PSF, and was masked out.

Spectral continuum fitting was performed using MPDAF on each spaxel over a velocity range of 1000 km s^{-1} around the emission and/or absorption lines of interest using zero-order polynomial functions. We found that this setup provided an optimal balance between accuracy and robustness of the results. The contribution of the sky background to the signal was estimated within concentric elliptical apertures around each object and subtracted from the signal measured in each spaxel.

The significance of the object's signal in each spaxel was assessed based on either the S/N ratio of the spectrum in the continuum adjacent to the line or the total S/N ratio of the spectrum in the searched window after continuum subtraction, depending on whether the feature to be mapped was an absorption or an emission line, respectively. For absorption lines, we focussed on the Mg II/Mg I lines near 2800 \AA (rest frame) and set a minimum S/N ratio of 2.0 per pixel in the dispersion direction to ensure that the object's continuum is bright enough to constrain the absorption lines (if any). This threshold corresponds to the detection of the three lines combined at the 5σ confidence level. The chosen parameters also enabled us to detect the Mg II signal on top of the quasar continuum, in spite of its faintness. For emission lines, we used a minimum S/N ratio of 1.0 per pixel in the dispersion direction around [O II] after continuum subtraction, which translates to a 4σ detection limit for a line spread over 15-20 pixels. Spaxels that did not meet these criteria were not considered any further.

We utilised PySpecKit (Ginsburg et al. 2022) for line fitting. To ensure robustness, we employed double Gaussian profiles with identical redshifts and spectral line widths to model the [O II] $\lambda\lambda 3727, 3729$ emission line doublet. Likewise, we used a single Gaussian profile for each of the three Mg lines with fixed wavelength ratios and identical line widths. In instances of non-detection, we established upper limits on rest-frame equivalent widths based on the root mean square (RMS) of the noise in the adjacent continuum. The resulting 2D maps of equivalent widths, line-of-sight velocities, and velocity dispersion, are shown in the image plane in Fig. D.1. We then applied the deflection matrices (see Sect. 3.2) to the positions of the spaxel corners (i.e., vertices) in the image plane to recover their delensed positions in the absorber plane. This leads to the maps shown in Fig. D.2.

The spatial resolution of these maps is constrained by the image quality, and this effect is not corrected before transforming the object geometries to the absorber plane. As a result, G2 appears more elongated in the southeastern-northwestern direction in the delensed maps than it is in reality. Additionally, due to the geometrical effects of lensing, Ci1 samples a narrow range in R.A. within the absorber plane, forming a slender, north-south elongated structure that is hardly visible on the absorption-line maps. The region of maximum velocity dispersion in G1's core can be used to derive the coordinates of G1's centre in the absorber plane, i.e., R.A. (J2000) = $0^{\text{h}} 33^{\text{m}} 40^{\text{s}}.91$, Dec. (J2000) = $+2^{\circ} 42' 22''.3$. The distribution of velocities along G1's major axis is found to turn around, changing from negative to positive values, at this position for $z_{\text{sys}} = 1.16677$.

Overall, we find no indication that the velocity measurements derived from emission or absorption lines are affected by lower S/N ratios. On the other hand, the determinations of gas velocity dispersion (i.e., line widths) exhibit considerable scatter, and their reliability is likely diminished in spaxels with weak absorption and/or noisy spectra.

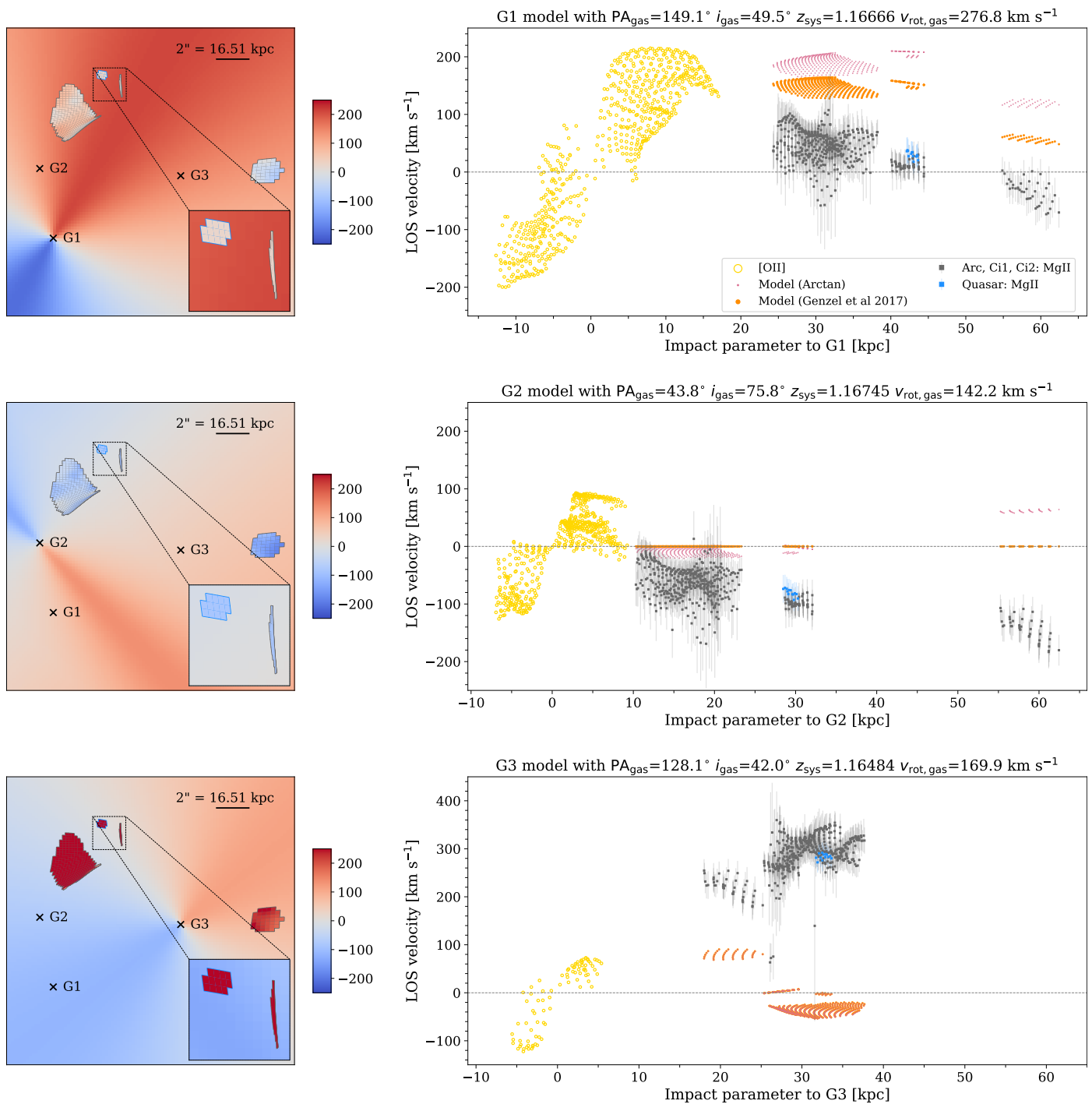


Fig. D.3: Single extended rotating disc models for G1, G2, and G3 (top, middle, and bottom panels, respectively) based on extrapolations of their [O II] kinematics. *Left panels:* Modelled velocity maps assuming arctangent rotation curves. The observed intervening Mg II mean velocities are overlaid for each of the four delensed sources. The inset shows a zoom-in on a region encompassing Ci1 and the quasar. *Right panels:* Model-predicted velocities for both the arctangent and realistic rotation curves (in pink and orange, respectively) at the positions of the Arc, Ci1, Ci2, and the quasar, as a function of impact parameter relative to the galaxy. The observed Mg II velocities are displayed in black for the Arc, Ci1, and Ci2, and in blue for the quasar.